Cell

Article

Persistent T cell activation and cytotoxicity against glioblastoma following single oncolytic virus treatment in a clinical trial

Graphical abstract

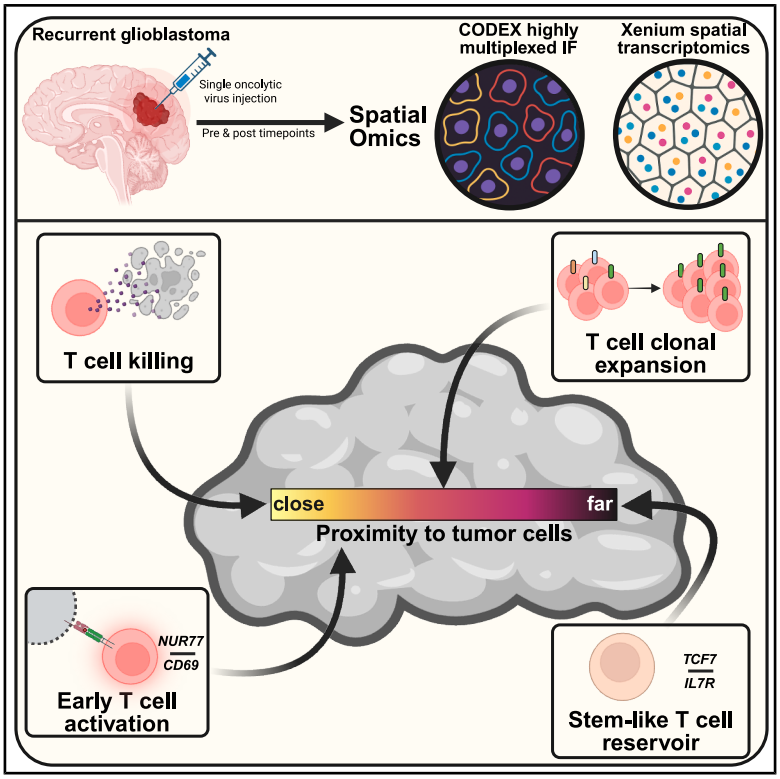

Highlights

- Oncolytic virus treatment induces deep and persistent T cell infiltration in human GBM
- Proximity of granzyme B^{+} CD8 T cells to apoptotic tumor cells correlates with patient survival
- Pre-existing tumor-infiltrating T cells expand upon oncolytic virus treatment
- Spatial TCR mapping shows continued engagement of GBM cells by expanded T cells

Authors

Maxime Meylan, Ye Tian, Lijian Wu, ..., Mario L. Suvà, E. Antonio Chiocca, Kai W. Wucherpfennig

Correspondence

suva.mario@mgh.harvard.edu (M.L.S.), eachiocca@mgb.org (E.A.C.), kai_wucherpfennig@dfci.harvard.edu (K.W.W.)

In brief

Single oncolytic virus treatment in patients with glioblastoma induces deep and persistent T cell activation against tumor cells. Direct and sustained T cell engagement with tumor cells upon treatment correlates with survival outcome.

Meylan et al., 2026, Cell *189*, 1287–1304
March 5, 2026
https://doi.org/10.1016/j.cell.2025.12.055

CellPress

Cell

CellPress
OPEN ACCESS

Article

Persistent T cell activation and cytotoxicity against glioblastoma following single oncolytic virus treatment in a clinical trial

Maxime Meylan,[1,2,10] Ye Tian,[1,2,10] Lijian Wu,[1,2,10] Alexander L. Ling,[3,10] Daniel Kovarsky,[4] Graham L. Barlow,[1,2] Linh D. Nguyen,[1] Jason Pyrdol,[1] Sascha Marx,[1,2] Lucas Westphal,[1] Julius Michel,[1,5,6] L. Nicolas Gonzalez Castro,[7,8] Sydney Dumont,[7,8] Andres Santos,[3] Itay Tirosh,[4] Mario L. Suvà,[7,8,*] E. Antonio Chiocca,[3,*] and Kai W. Wucherpfennig[1,2,9,11,*]

[1]Department of Cancer Immunology and Virology, Dana-Farber Cancer Institute, Boston, MA, USA
[2]Department of Immunology, Harvard Medical School, Boston, MA, USA
[3]Harvey Cushing Neuro-Oncology Laboratories, Department of Neurosurgery and Center for Tumors of the Nervous System, Neuroscience Institute and Cancer Institute, Mass General Brigham, Boston, MA, USA
[4]Department of Molecular Cell Biology, Weizmann Institute of Science, Rehovot, Israel
[5]Heidelberg Institute for Stem Cell Technology and Experimental Medicine (HI-STEM), Heidelberg, Germany
[6]German Cancer Research Center (DKFZ), JRG Hematology and Immune Engineering, Heidelberg, Germany
[7]Department of Pathology and Krantz Family Center for Cancer Research, Massachusetts General Hospital, Boston, MA, USA
[8]Broad Institute of MIT and Harvard, Cambridge, MA, USA
[9]Department of Neurology, Brigham and Women's Hospital, Boston, MA, USA
[10]These authors contributed equally
[11]Lead contact
*Correspondence: suva.mario@mgh.harvard.edu (M.L.S.), eachiocca@mgb.org (E.A.C.), kai_wucherpfennig@dfci.harvard.edu (K.W.W.)
https://doi.org/10.1016/j.cell.2025.12.055

SUMMARY

A recent first-in-human clinical trial demonstrated that survival in glioblastoma (GBM) patients following rQNestin34.5v.2 oncolytic virus treatment was associated with immune activation signatures. This study was registered at ClinicalTrials.gov (NCT03152318). Here, we provide *in situ* evidence of ongoing T cell-mediated cytotoxicity against tumor cells at late time points following single treatment, with deep and persistent T cell infiltration into tumor regions. Shorter distances between cleaved caspase-3$^+$ tumor cells and granzyme B$^+$ T cells were associated with longer progression-free survival following treatment. Pre-existing tumor-infiltrating T cells expanded locally upon treatment, correlating with longer overall patient survival. T cells with an early activation program closely interacted with tumor cells and were strongly enriched upon treatment. Viral remnants were restricted to necrotic regions, while T cells infiltrated deeply into live tumor regions. These data demonstrate that single oncolytic virus treatment can expand pre-existing T cell clones and trigger persistent T cell-mediated immunity against GBM.

INTRODUCTION

The development of targeted therapies and immunotherapies for glioblastoma (GBM) has proven to be challenging due to the remarkable genetic heterogeneity and plasticity of malignant cells. Plasticity has hindered the development of targeted therapies partly because malignant cells can shift between neural-precursor-like (NPC-like), oligodendrocyte-like (OPC-like), astrocyte-like (AC-like), and mesenchymal-like (MES-like) cellular states.[1] A repertoire of T cells targeting diverse tumor antigens could potentially deal with such tumor cell heterogeneity, but some of these GBM cell states evade immune recognition by downregulation of major histocompatibility complex (MHC) class I molecules and expression of ligands for inhibitory receptors on T cells, including PD-L1 (programmed cell death 1 [PD-1]), CLEC2D (CD161), and CD155 (T cell immunoreceptor with Ig and ITIM domains [TIGIT]).[1–4] Clinical trials with immune checkpoint blockers active in multiple other cancer types have yielded negative results in GBM.[5–7] The fundamental challenge is that GBM is poorly infiltrated by T cells, and the sparsely infiltrating T cells are primarily residing in perivascular spaces rather than infiltrating deeply into tumor regions.[2] Therefore, it is important to develop therapeutic interventions that enable deep and sustained T cell infiltration in GBM as the foundation of combination therapies.

Oncolytic viruses have generated significant interest based on their selective replication in cancer cells and induction of immunogenic cell death.[8] Oncolytic viruses based on herpes simplex

virus type 1 (oHSV-1) were the first to be evaluated in clinical trials. The FDA has approved an oHSV-1 virus, Talimogene laherparepvec (T-VEC), for the treatment of unresectable stage IIIB-IV melanoma. A significant difference in overall survival was observed in melanoma patients with stage III-IVM1a disease: 46.8 months in the T-VEC arm compared with 21.5 months in the granulocyte macrophage-colony stimulating factor (GM-CSF) arm.[8,9] Teserpaturev (G47Δ) was approved in Japan for the treatment of recurrent GBM (rGBM) based on a phase 2 clinical trial in which the virus was administered intratumorally up to six times.[10] It is a genetically engineered oHSV-1 in which the *ICP34.5* (neurovirulence factor), *ICP47* (inhibitor of antigen presentation), and *ICP6* (viral replication) genes were inactivated. The clinical trial leading to regulatory approval demonstrated increased densities of $CD4^+$ and $CD8^+$ T cells following repeated virus injection, but there is a very limited understanding of the functional states and spatial interactions of the induced T cell populations.[10]

In a recently reported first-in-human clinical trial in rGBM (clinicaltrials.gov, arm A of NCT03152318), we evaluated rQNestin34.5v.2 (CAN-3110, linoserpaturev), an oHSV-1 in which expression of the viral *ICP34.5* gene was controlled by the nestin promoter, a gene overexpressed in GBM.[11] Post-treatment resections showed increased T cell infiltration, with T cell receptor (TCR)β-based T cell fraction correlating with survival independently of HSV-1 serology.[11] These clinically relevant findings motivated this study, which sought to develop a deeper mechanistic understanding of T cell programs following oHSV treatment using highly multiplexed spatial proteomics (CODEX) and spatial transcriptomics (Xenium) technologies.

RESULTS

Deep, persistent T cell infiltration following a single oncolytic virus injection

The goal of this study was to investigate the spatial interactions of T cells with tumor and other immune cells using CODEX[12] and Xenium[13] technologies on tissue specimens from arm A of the phase 1 rQNestin34.5v.2 clinical trial.[11] CODEX was used to visualize and quantify ongoing T cell-mediated cytotoxicity against GBM cells based on the proximity of granzyme B-positive ($GZMB^+$) CD8 T cells and cleaved caspase-3 positive ($cl\text{-}Casp3^+$) tumor cells. TCR repertoire analysis in tumor and blood specimens at pre- and post-treatment time points was used to identify treatment-expanded T cell clones. Such expanded TCR clonotypes were spatially mapped *in situ* with a high degree of specificity using the Xenium spatial transcriptomics platform, enabling visualization of early T cell activation programs in expanded T cells that closely interacted with tumor cells (Figure 1A). We established a 27-marker CODEX panel for detailed characterization of immune, stromal, and cancer cell states (Tables S1 and S2). We imaged 28 large tumor regions from 16 post-treatment cases, leading to the clustering and annotation of 3.8 million cells belonging to 11 cell types (Figures S1A and S1B) and 21 regions from 16 pre-treatment biopsies (Figure S1C). Consistent with Ling et al.,[11] we observed that oHSV treatment resulted in a substantial increase in GBM infiltration by CD8 T cells, CD4 T cells, and B cells (Figures 1B and 1C). An increase in $FoxP3^+$ CD4 T regulatory cells was also observed, likely driven by the lymphocyte influx (Figure 1C). However, CD8 T cells expanded to a greater extent than regulatory T cells, resulting in a significant increase in the CD8/regulatory T cell (Treg) ratio from pre- to post-treatment (median ratio: 6.8 pre versus 21.1 post, $p = 0.0042$, paired Wilcoxon test) (Figure S1D). Notably, we detected formation of lymphoid aggregates (Figure 1Ba) as well as deep T cell infiltration into tumor regions (Figure 1Bb) in samples collected at long time intervals post-oHSV treatment (Figure 1B). CD8 and CD4 T cell densities relative to time from oHSV injection showed high variability between cases at early time intervals (months 0 to 3). Substantial T cell infiltration was observed for long time intervals following single oHSV injection (months 6 to 25), including for >2 years in one patient (Figure 1D). Elevated T cell infiltration was observed across collection time points and oHSV doses, including the lowest dose range (Figures 1E and S1E).

To further investigate dynamic changes in T cells, tumor molecular profiles, and the presence of HSV, Xenium spatial transcriptomics analysis was performed on paired pre- and post-oHSV samples from eight patients. A 380-gene immuno-oncology panel was complemented with 100 custom probes targeting (1) early T cell activation markers (including *NR4A1* and *CD69*),[14] (2) 50 expanded TCR clonotypes identified in pre- and/or post-oHSV samples, (3) GBM malignant cell states,[1] and (4) key HSV genes (*ICP4*, *ICP22*, *ICP27*, *ICP34.5*, and *gC*). A total of 2.4 million cells were clustered and annotated as 11 cell types (Figures S1F and S1G). Parallel quantification of T cells with Xenium demonstrated similar enrichment post-treatment, with a median density of 30.4 cells/mm^2 in pre- versus 138 cells/mm^2 in post-treatment samples ($p = 0.0078$) (Figure S1H).

Spatial evidence of T cell-mediated cytotoxicity against GBM cells

In post-oHSV samples, we observed extensive T cell infiltration into the tumor parenchyma at late time points following treatment, as illustrated for two representative patients (P28 and P34) at 253 and 100 days post-oHSV treatment, respectively (Figures 2A and S2A). CODEX imaging revealed robust infiltration by both $CD4^+$ (green) and $CD8^+$ (magenta) T cells penetrating deeply into $GFAP^+$ (blue) tumor regions. T cells formed dense clusters in lymphoid aggregates (Figure 2Aa1), while deeper into tumors, T cell infiltration varied markedly between subregions, with areas of high T cell densities (Figure 2Aa2) or sparse infiltration (Figure 2Aa3). T cell infiltration was quantified using two complementary maps: (1) a continuous color map showing $CD3\varepsilon^+$ cell density (top middle) and (2) a bivariate color map (top right) depicting T cell-tumor co-localization or exclusion (Figures 2A and S2A). Robust T cell infiltration was confirmed in additional samples collected between 24 and 331 days following oHSV injection (Figure 2B). These findings were confirmed by spatial transcriptomics, which showed close contact between T cells (red) and tumor cells (blue) in different tumor areas (Figures 2Ca–2Cd, S2Be, and S2Bf). Other T cell populations were localized in lymphoid niches adjacent to vasculature (Figure S2B, zoom regions g and h).

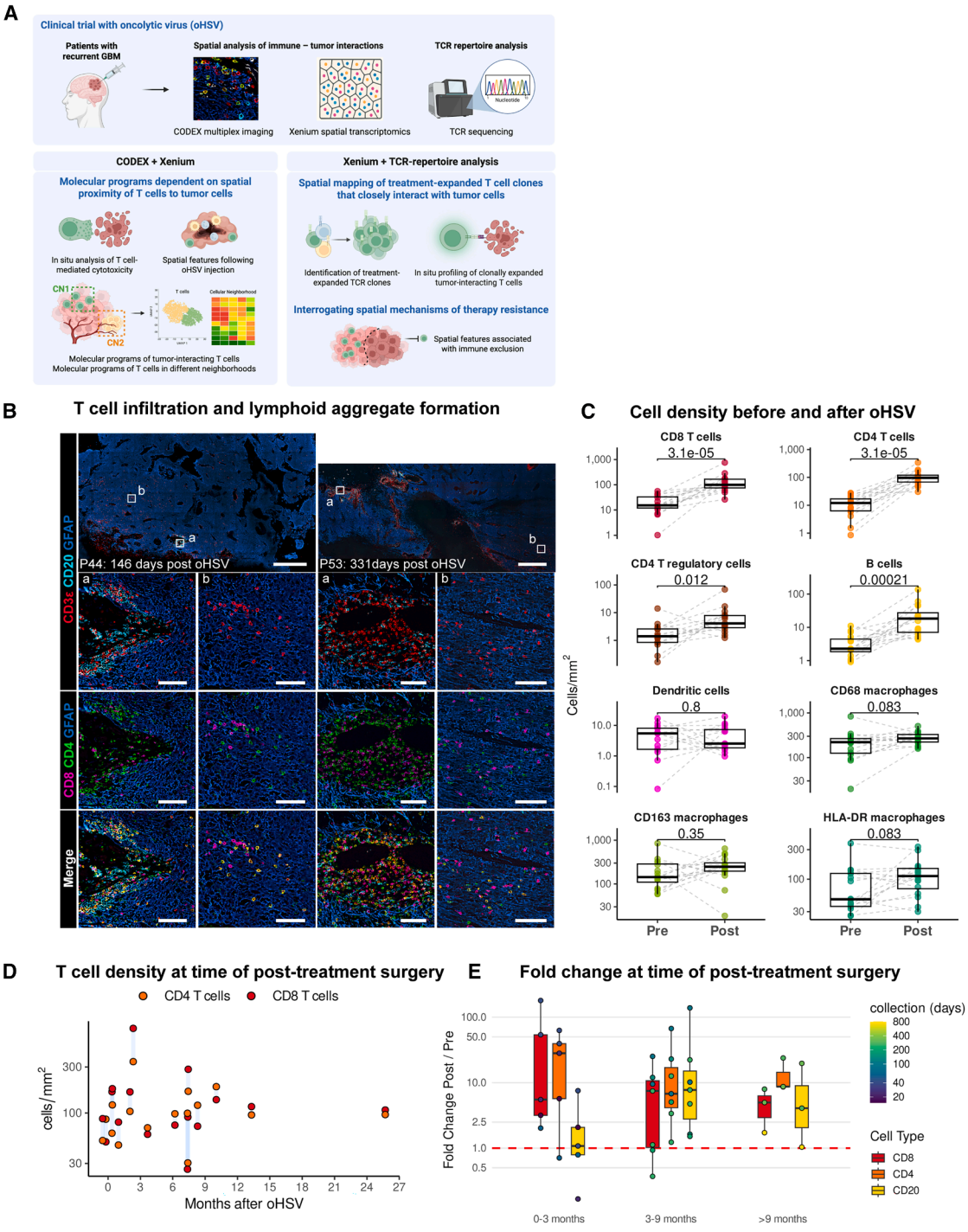

Figure 1. Persistent deep T cell infiltration after single oncolytic virus treatment

(A) Cartoon summary of study design.

(B) CODEX images from two post-treatment resections (146 and 331 days) showing lymphoid aggregates (a) and deep CD8$^+$ and CD4$^+$ T cell penetration into the GFAP$^+$ tumor bed (b).

Scale bars: 1 mm (top row) and 100 μm (regions a and b).

(C) Boxplots of immune cell densities in paired pre- versus post-treatment samples measured by CODEX ($\log_{10}$ cells/mm^2). Wilcoxon signed-rank p values are shown.

(D) Scatterplot of CD8 and CD4 T cell densities versus months after treatment.

(E) Fold-change in T cell density (post/pre, CODEX, $\log_{10}$ scale) versus time after treatment, colored by collection time.

See also Figure S1.

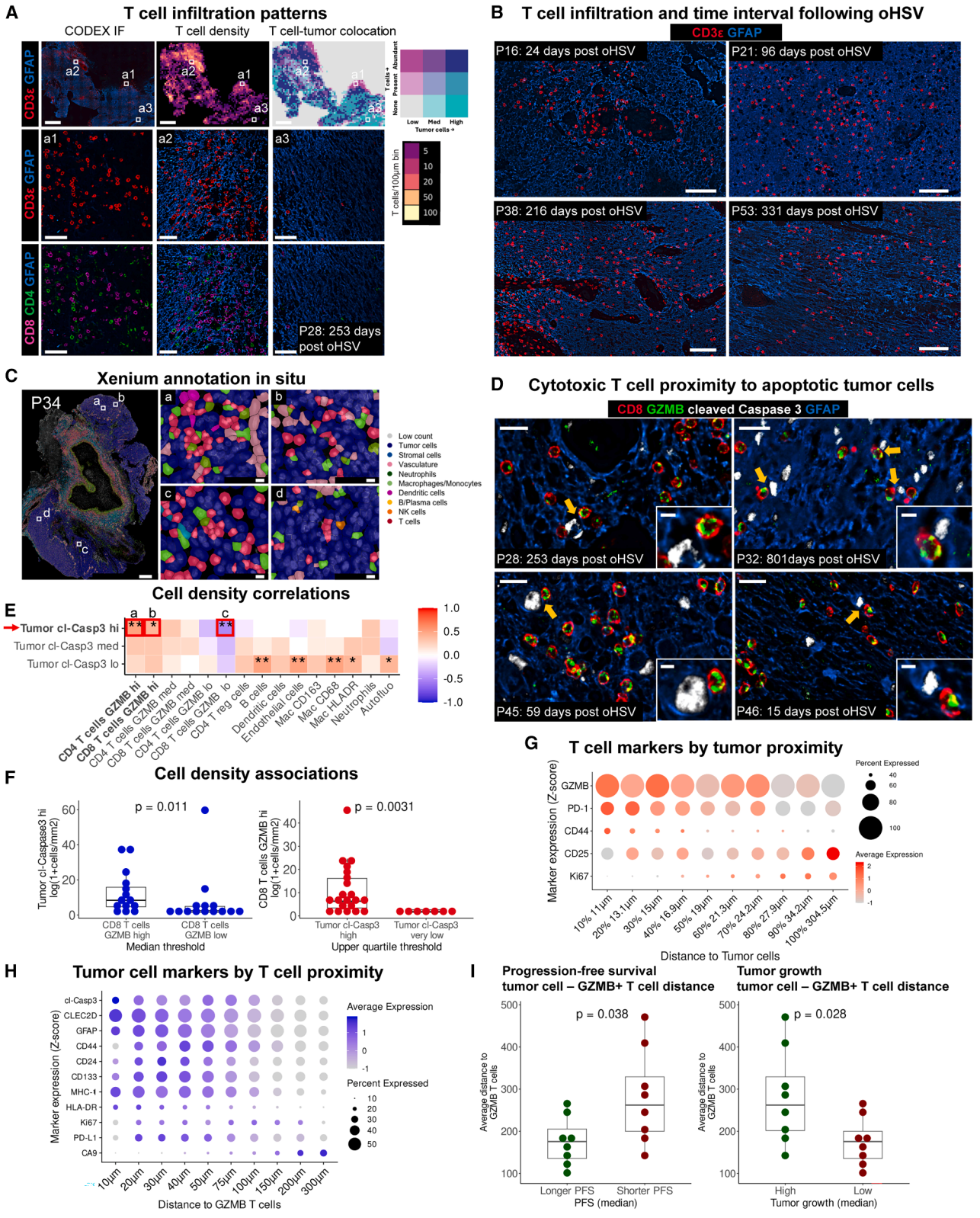

(legend on next page)

Importantly, we captured GZMB^{+} T cells in close proximity to apoptotic cl-Casp3^{+} tumor cells *in situ* (yellow arrows in Figure 2D). This pattern was observed across multiple specimens and is consistent with cytotoxic activity of GZMB^{+} T cells against tumor cells. To quantify interactions between T cells and apoptotic tumor cells, T cells and tumor cells were stratified by GZMB and cl-Casp3 expression intensity (Figure S2C). First, cell densities were computed for each GZMB T cell and cl-Casp3 tumor category. GZMB^{hi} CD8^{+} and CD4^{+} T cells were the only cell populations that positively correlated with cl-Casp3^{hi} tumor cells (r = 0.4, p = 0.035 and r = 0.5, p = 0.007, respectively) (Figures 2E, S2Da, and S2Db). By contrast, GZMB^{lo} CD8^{+} T cells were negatively correlated with the density of cl-Casp3^{hi} tumor cells (r = −0.5, p = 0.007) (Figure S2Dc). The time of sample collection did not seem to have an impact on the observed correlation (Figure S2D). Cl-Casp3^{hi} tumor cell density was higher in samples with a higher density of GZMB^{hi} CD8 T cells (10 versus 3 cells/mm^2, p = 0.011) (Figure 2F). Conversely, samples with a higher density of cl-Casp3^{hi} tumor cells (upper quartile) had a higher density of GZMB^{hi} CD8 T cells (8 versus 2 cells/mm^2, p = 0.0031) (Figure 2F, right).

We quantified the spatial relationships between GZMB$^{hi\text{-}med}$ T cells and tumor cells using a nearest-neighbor analysis approach, which revealed distinct gradients in both T cell and tumor cell states. GZMB, PD-1, and CD44 levels were highest in T cells located close to tumor cells (Figure 2G), consistent with an antigen-experienced cytotoxic phenotype (p = 0.016) (Figure S2E). By contrast, GZMB^{lo} CD25^{+} T cells were located at larger distances from tumor cells and enriched in lymphoid niches (Figure 2G). T cells in these lymphoid niches showed higher levels of Ki67 (p = 0.026) (Figure S2E), indicative of active proliferation in these microenvironments. These patterns were apparent when averaging values per distance bin across all samples (Figure S2F).

To explore how tumor cells were shaped by proximity to T cells, we performed a reciprocal spatial analysis examining tumor cell marker expression based on distance to GZMB$^{hi\text{-}med}$ T cells. Analysis of tumor marker expression across distance categories revealed distinct gradients dependent on proximity to T cells (Figure 2H). Tumor cells in close contact with GZMB$^{hi\text{-}med}$ T cells showed significant expression of cl-Casp3 (apoptosis), CLEC2D (CD161 ligand, immune evasion), MHC-I (antigen presentation), and GBM tumor markers. Conversely, more distant tumor cells exhibited higher CA9 levels, a marker of hypoxic regions.[15] Of note, the distribution of tumor cells across these T cell-specific distance bins was not uniform, and most tumor cells were in the ≥300 μm distance bin (Figure S2G). Detailed examination of MHC-I and CA9 expression (Figure S2H) demonstrated opposing patterns, with significantly higher MHC-I levels in tumor cells located closer to T cells (p = 0.00016), while CA9 expression progressively increased with greater distance from T cells (p = 8.7e−06), peaking in areas furthest from infiltrating GZMB$^{hi\text{-}med}$ T cells. These inverse relationships were maintained when averaging values across distance bins (Figure S2I), with expression patterns crossing at a distance of ∼85 μm from T cells, suggesting a critical distance for T cell interaction and tumor adaptation within the microenvironment.

To assess the clinical and biological relevance of this spatial metric, we examined whether the proximity between GZMB$^{hi\text{-}med}$ T cells and tumor cells correlated with patient outcome and tumor growth (n = 16 patients). This spatial relationship was correlated with progression-free survival (PFS): patients with above-median PFS exhibited shorter T cell-tumor cell distances (175 μm versus 262 μm, p = 0.038) (Figure 2I, left), consistent with more effective T cell-mediated tumor immunity. The functional relevance of this metric was further supported by its correlation with tumor growth: shorter GZMB$^{hi\text{-}med}$ T cell-tumor cell distances were associated with lower tumor growth rates following oHSV injection (p = 0.028) (Figure 2I, right).

Molecular evidence of early activation and tissue-residency programs in tumor-interacting T cells

To further characterize T cell functional states following oHSV treatment, we analyzed our Xenium dataset for key T cell programs: early activation (*NR4A1*/Nur77, *CD69*, *IFNG*, and *TNF*), tissue residency (*ITGAE*/CD103 and *ZNF683*/HOBIT), cytotoxicity (*PRF1*, *GZMB*, *GZMA*, *GNLY*, and *GZMK*), proliferation

Figure 2. Evidence of *in situ* cytotoxicity by GZMB^{+} T cells against GBM cells

(A) CODEX composite of P28 (253 days post oHSV) with three regions of interest (ROIs): (a1) lymphoid aggregate, (a2) tumor-T cell interaction, (a3) tumor core. Center: CD3ε^{+} T cell density heatmap (cells per 100 μm^2). Right: bivariate T cell versus tumor cell density, highlighting spatially heterogeneous yet deeply infiltrating T cell population. Scale bars: 1 mm (top row) and 50 μm (regions a1–a3).

(B) Additional CODEX fields from four cases illustrating deep T cell infiltration into tumor regions.

Scale bars: 100 μm.

(C) Xenium images from P34 (day 100) showing T cells (red) interacting with tumor cells (blue) across zooms a–d. Scale bars: 1 mm (left panel) and 10 μm (regions a–d).

(D) CODEX: CD8^{+} T cells (red) expressing GZMB (green) adjacent to cl-Casp3^{+} tumor cells (white), providing evidence for ongoing cytotoxicity (yellow arrows) at multiple time points post-oHSV. Scale bars: 20 μm (large field of view) and 5 μm (zoom).

(E) Pairwise Spearman correlation heatmap (CODEX) between immune subsets and cl-Casp3^{hi} tumor-cell density. Individual correlations (a–c) are shown in Figure S2D. Spearman's r and p values are shown.

(F) Boxplots of CODEX cell densities. Left: cl-Casp3^{hi} tumor cell density (cells/mm) stratified by GZMB^{hi} CD8^{+} T cell density (median threshold). Right: GZMB^{hi} CD8^{+} T cell density stratified by cl-Casp3^{hi} tumor cell density (upper quartile).

(G) Dot plot of T cell markers based on proximity to tumor cells.

(H) Dot plot of tumor cell markers based on proximity to T cells.

(I) Correlation of PFS (left) and tumor growth rate (right) with average distance of tumor cells to GZMB^{hi} T cells (n = 16 patients). Wilcoxon rank-sum p values are shown.

See also Figure S2.

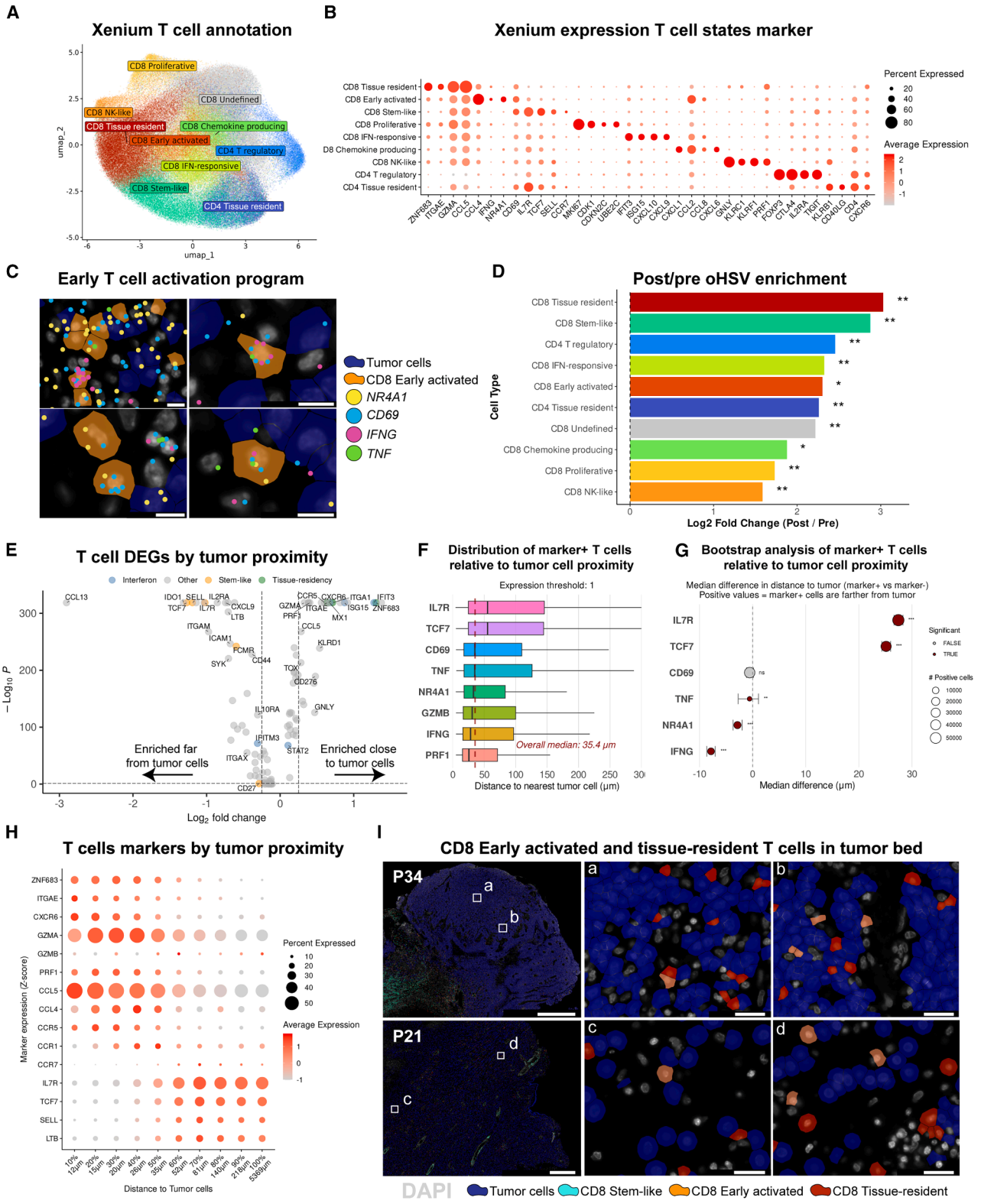

Figure 3. Molecular characterization of tumor-infiltrating T cells

(A) UMAP of 10 T cell subclusters.

(B) Dot plot of key marker genes for each CD8 and CD4 T cell state.

(legend continued on next page)

(*MKI67* and cell cycle genes), stem-like state (*SELL*, *CCR7*, *TCF7*, and *IL7R*), interferon pathway (*IFNA1*, *ISG15*, and *STAT1*), and exhaustion (*PDCD1*/PD-1, *LAG3*, and *TOX*). Quantification revealed significant post-treatment enrichment of T cells with such molecular programs (Figure S3A). Unsupervised clustering identified 12 distinct T cell clusters, consolidated into 8 $CD8^+$ and 2 $CD4^+$ states (Figures 3A, 3B, and S3B–S3D).

We identified a subset of $CD8^+$ T cells exhibiting hallmarks of recent TCR engagement through expression of *NR4A1*/NUR77 and *CD69*. This population was also enriched in expression of *IFNG* and *TNF* cytokine and *CCL3* and *CCL4* chemokine genes (Figure S3D, red box). *NR4A1*/NUR77 is one of the earliest transcription factors upregulated following TCR activation, providing evidence of persistent tumor antigen recognition.[14,16] Spatial co-localization analysis confirmed that these activation markers were co-expressed within T cells in close contact with tumor cells (Figure 3C).

Post-treatment samples showed dramatic expansion of all T cell populations compared with pre-treatment specimens, with $CD8^+$ tissue-resident T cells exhibiting the most pronounced increase (average log2FC = 3.03), followed by $CD8^+$ stem-like T cells (average log2FC = 2.87) and $CD4^+$ regulatory T cells (average log2FC = 2.46, all $p = 0.0078$) (Figures 3D and S3E). The proportional representation of different T cell states was similar across post-treatment samples, with $CD8^+$ tissue-resident cells comprising ~16% and early activated $CD8^+$ T cells representing ~5% of the total T cell population (Figure S3F). To determine how T cell states were influenced by spatial context, we quantified distances between T cells and tumor cells using the approach described in Figure 2. Opposing spatial gradients of gene expression were observed in T cells above versus below the median distance (35.4 μm) to tumor cells. T cells located closer to tumor cells showed enrichment of tissue-residency (*ITGAE*/CD103, *ZNF683*/HOBIT, and *CXCR6*)[17] and interferon-inducible (*IFIT3*, *ISG15*, and *MX1*) genes, while stem-like features (*SELL*, *TCF7*, and *IL7R*) gradually increased with larger distances from tumor cells (Figure 3E).

Examination of the spatial distribution of T cells expressing specific markers (≥1 count) revealed striking organization relative to tumor cells (Figure 3F). T cells positive for early activation markers were located closer to tumor cells, with median distances below the overall median (35.4 μm) for $PRF1^+$, $IFNG^+$, $GZMB^+$, and *NR4A1*/$Nur77^+$ cells. By contrast, T cells expressing stem-like markers were positioned further away from tumor cells. Bootstrap analysis comparing marker-positive versus marker-negative T cells (Figure S3G) confirmed these spatial preferences, with activation markers (*NR4A1*, *CD69*, *IFNG*, and *TNF*) consistently enriched in tumor-proximal regions. Statistical comparisons showed significant differences ($p < 0.001$) for all markers except CD69: T cells with activation markers ($IFNG^+$ and $NR4A1^+$) were 7.8 and 2.8 μm closer, while cells with stem-like markers ($IL7R^+$ and $TCF7^+$ cells) were 27.4 and 25.1 μm farther from tumor cells (Figure 3G).

This spatial organization extended systematically across additional functional markers, with tissue-residency genes (*ZNF683*/HOBIT, *ITGAE*/CD103, and *CXCR6*) and cytotoxic molecules (*GZMA*, *GZMB*, and *PRF1*) showing the highest expression in tumor-proximal regions and gradually decreasing with distance. Notably, expression of chemokines *CCL4* and *CCL5* and their *CCR5* and *CCR1* receptors was prominent in T cells in close proximity to tumor cells, consistent with a chemokine-mediated mechanism by which activated T cells recruit additional T cells into tumor regions.[18] By contrast, stem-like markers (*IL7R*, *TCF7*, and *SELL*) displayed the inverse gradient, with expression progressively increasing at greater distances from tumor cells (Figure 3H). Visual examination confirmed these patterns, with early activated and tissue-resident T cells embedded within tumor regions (Figure 3I). This spatial polarization of T cells with early activation markers near tumor cells provides strong evidence for ongoing tumor antigen recognition and TCR engagement following oHSV therapy.

Spatial compartmentalization of the T cell response following oHSV

Following oHSV treatment, we observed robust immune cell infiltration across multiple lineages (Figure S4A) in the Xenium dataset. Plasma cells showed the strongest enrichment (log2FC = 3.47, $p = 0.0156$) in post- versus pre-treatment samples, followed by T cells (log2FC = 2.91, $p = 0.0078$). Among myeloid cells, only dendritic cells showed enrichment (log2FC = 1.46, $p = 0.0078$) (Figure S4B).

Immune infiltration exhibited remarkable spatial organization: $CD8^+$ tissue-resident and early activated T cells localized near tumor cells, while $CD8^+$ stem-like T cells were distant (Figure 4A). Quantitatively, when comparing T cells in close contact with tumor cells (0%–20%; 0–15 μm) versus those most distant (80%–100%; 140–5,369 μm), we observed over 5-fold enrichment of IFN-responsive and early activated CD8 T cells ($p = 0.0156$ and $p = 0.0391$) followed by tissue-resident CD8 T cells (fold change = 2.2, $p = 0.0391$) in the tumor-proximal zone, while stem-like CD8 T cells were 1.75-fold depleted from these regions ($p = 0.0234$) (Figure 4B).

We next performed cellular neighborhood (CN) analysis, identifying 14 clusters consolidated into eight functional zones

(C) Early T cell activation program and $NR4A1^+$ CD8 T cells in close contact with tumor cells for post-treatment sample P34 (Xenium). Scale bars: 10 μm.
(D) Post- versus pre-oHSV enrichment of T cell states. Log2 fold changes tested against zero using Wilcoxon signed-rank test.
(E) Differential gene expression in T cells closer (<35 μm) versus more distant (≥35 μm) to tumor cells by Xenium. Adjusted Wilcoxon rank-sum *p* values are shown.
(F) Spatial distribution of activation, residency, and stem-like marker-positive T cells (≥1 transcript) by distance to tumor cells.
(G) Median tumor-proximity difference between marker-positive and marker-negative T cells. Median differences with 95% bootstrap confidence intervals are shown; adjusted Wilcoxon rank-sum *p* values are shown.
(H) Dot plot of T cell gene expression gradients across tumor cell proximity bins.
(I) Xenium image illustrating spatial localization of early activated and tissue-resident T cells infiltrating into tumor areas for post-treatment samples. Scale bars: 1 mm (left panels) and 25 μm (regions a–d).
See also Figure S3.

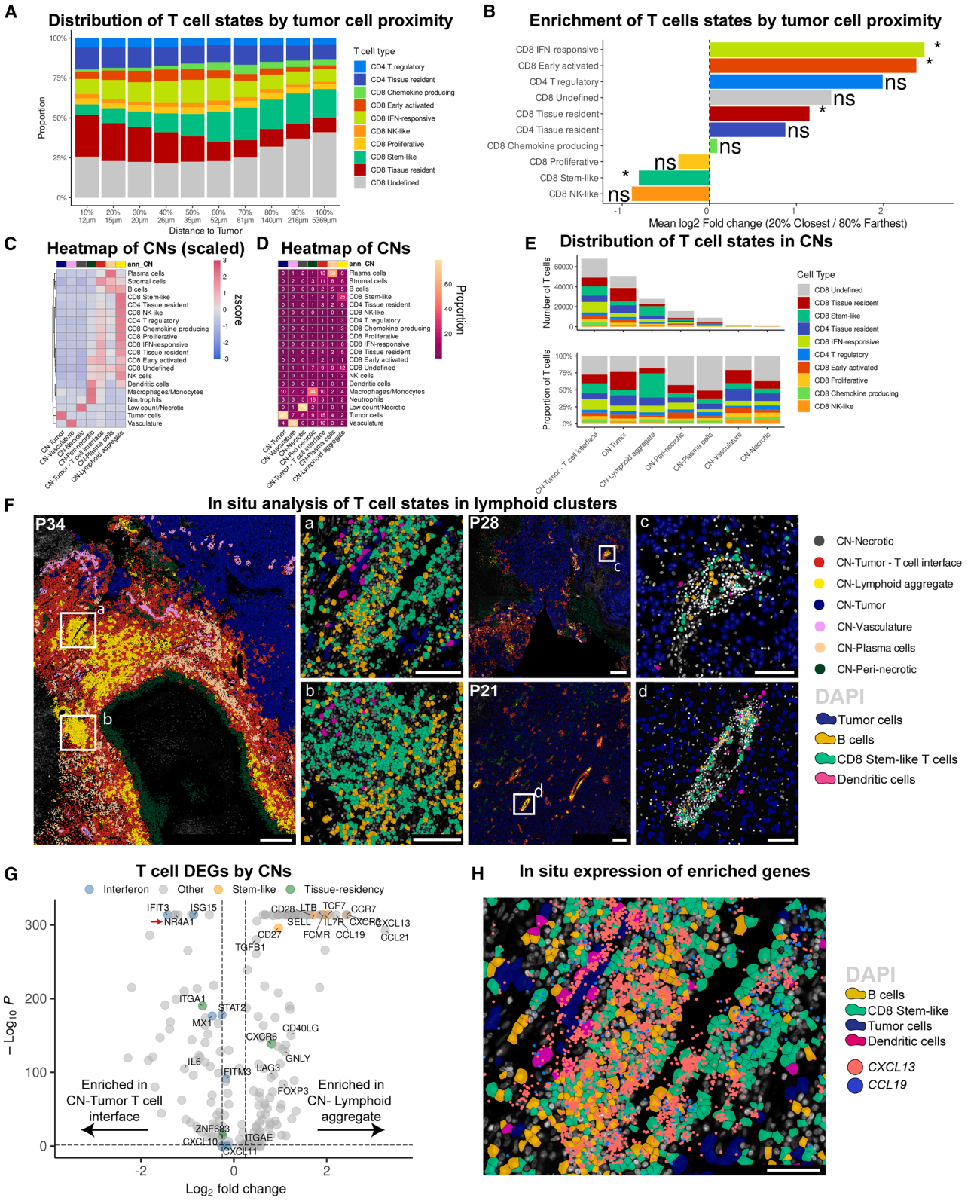

(legend on next page)

(Figures 4C and 4D): tumor, tumor-T cell interface, plasma cell, lymphoid aggregate, vasculature, peri-necrotic, and necrotic regions. The largest T cell compartment (~40%) corresponded to the tumor-T cell interface, followed by tumor (30%) and lymphoid aggregate (16%) CNs (Figure 4E). Within lymphoid aggregates, 35% of T cells were stem-like $CD8^+$ cells, closely interacting with B cells and dendritic cells (Figure 4F). These stem-like T cells are associated more closely with B cells (56 μm) and dendritic cells (119 μm) than tissue-resident $CD8^+$ T cells (279 and 257 μm) (Figures S4F and S4G).

CN-lymphoid aggregate T cells upregulated lymphoid tissue organizing genes (*CXCL13*, *LTB*, and *CCL19*) and B cell/dendritic cell interaction markers (*CD40*, *CD28*, and ICOS). Conversely, T cells in the CN-tumor T cell interface expressed interferon, tissue residency, and the early activation markers (*NR4A1*, red arrow in Figure 4G). We confirmed robust expression of *CXCL13* and *CCL19* within lymphoid aggregates (Figure 4H). However, this neighborhood did not display canonical features of tertiary lymphoid structures because it lacked defined B and T cell zones and germinal center formation (Figure 4F).

To further evaluate the immunosuppressive landscape within these CNs, we analyzed the expression of inhibitory molecules by macrophages and monocytes according to their spatial location. Strikingly, myeloid cells expressed distinct sets of immunosuppressive molecules based on their neighborhood context (Figure S4H). In CN-lymphoid aggregates, macrophages/monocytes preferentially expressed *CLEC2D* and *TGFB1*, while those in the CN-tumor neighborhood exhibited high levels of *CD276* (B7-H3), *VEGFA* (vascular endothelial growth factor A), and *SPP1*.

CODEX analysis reproduced the same CNs (Figures S4I–S4K), including lymphoid aggregates of T, B, and dendritic cells; a tumor-T cell interface (47% tumor, 5% $CD8^+$ T cells); and peri-necrotic regions with macrophages and neutrophils. Tumor-infiltrating T cells showed cytotoxic ($GZMB^+$ $CD44^+$) profiles, while lymphoid-cluster T cells were proliferative ($Ki67^+$ and $CD44^-$) (Figure S4K).

Residual oncolytic virus restricted to necrotic tumor regions

We performed HSV immunohistochemistry (IHC) on formalin-fixed, paraffin-embedded (FFPE) sections consecutive to those used for CODEX analysis to localize oHSV, and 32.1% of regions (9/28) showed some labeling. We did not detect HSV staining in viable tumor regions. Rather, HSV antibody labeling was only observed in necrotic regions characterized by low or absent DAPI (DNA) signal, explaining the diffuse HSV antibody labeling in positive regions (Figure 5A). To identify which cell types were spatially associated with HSV-positive regions, we measured distances between cell types and HSV-positive areas detected by IHC. Quantitative spatial analysis revealed distinct immune cell compartmentalization around HSV^+ regions. Human leukocyte antigen (HLA)-DR^+ macrophages and neutrophils were enriched (log2FC > 1) in the immediate proximity to sites with residual HSV (0–50 μm interval). By contrast, both $CD8^+$ and $CD4^+$ T cells showed pronounced depletion from the same areas (log2FC = −3.47 and −2.01, respectively) (Figures 5B and S5A).

We further probed the presence of HSV nucleic acids by leveraging our custom Xenium panel, which included probes targeting 5 key HSV genes: the immediate-early genes (*ICP4*, *ICP22*, and *ICP27*), surface glycoprotein for viral entry (*gC*), and the neurovirulence factor (*ICP34.5*). HSV viral nucleic acids were detected in necrotic areas of 4 out of 8 post-treatment samples. Importantly, no robust HSV signal was detected in pre-treatment samples, even in HSV seropositive patients prior to oHSV injection (P21, P32, P34, and P46) (Figure 5C). In post-treatment sample P34, we identified a small focal necrotic region characterized by HSV transcripts but lacking viable cells, as evidenced by degraded nuclear staining that prevented cell segmentation (Figures 5C, red asterisks, and S5B, zoomed). Similarly, in post-treatment sample P05, HSV was detected at the tumor margin, adjacent to an area characterized by low transcript counts and degraded nuclear staining (Figure S5C).

Systematic quantification of HSV transcripts revealed that viral targets were detected in a subset of post-treatment samples, with most cells remaining HSV-negative. The highest viral positivity was observed in sample P05 (post), where HSV transcripts were detected in up to 25% of cells, again concentrated in regions with necrotic features and low overall transcript counts. All other samples had less than 1% positive cells (Figure S5D). When defining HSV-positive cells as those containing at least one viral transcript, we found enrichment in the tumor and low-count/necrotic compartment only in post-treatment samples, while other cell types showed background levels of viral RNA (Figure S5E).

We quantified distances between each cell type and HSV^+ regions (nearest 20 cells) (Figure 5D). Low-count/necrotic cells were closest (~120 μm median), while T and B cells were farthest (>200 μm). Cell-type proportions across distance intervals

Figure 4. Spatially organized CNs underpin coordinated immunity

(A) Distribution of T cell state proportions relative to tumor cell proximity.

(B) Log_2-fold enrichment of T cell states in proximal (0%–20%; 0–15 μm) versus distal bins (80%–100%; 140–5,369 μm) relative to tumor cells. Log2 fold changes tested against zero using Wilcoxon signed-rank test.

(C and D) Cell composition of Xenium-based CN analysis as normalized values (C) or proportions (D).

(E) Distribution of T cell states in CNs by total cell counts (top) or proportion (bottom).

(F) Xenium composite image showing stem-like CD8 T cells interacting with B cells and dendritic cell lysosome-associated membrane protein $(DC\text{-}LAMP)^+$ dendritic cells inside lymphoid aggregates in three post-treatment tumors. Scale bars: 500 μm (large overviews for P34, P28, and P21) and 100 μm (zooms a–d).

(G) Volcano plot representing differentially expressed genes between T cells in lymphoid aggregates or the tumor-T cell interface. Adjusted Wilcoxon rank-sum *p* values are shown.

(H) *In situ* Xenium image localizing *CXCL13* and *CCL19* transcripts within lymphoid aggregates. Scale bar: 50 μm.

See also Figure S4.

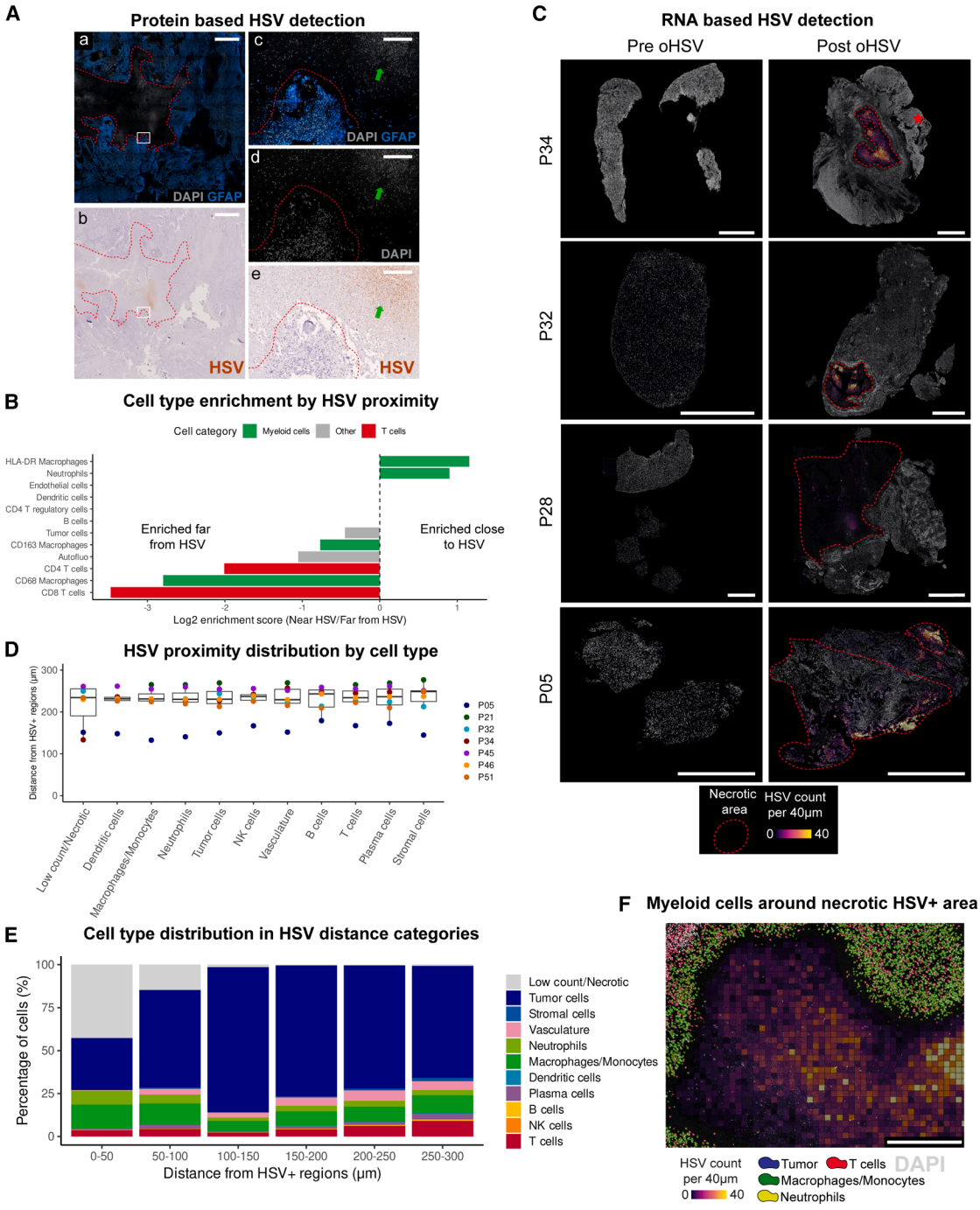

Figure 5. Residual oncolytic virus localizes to necrotic tumor regions

(A) IHC-CODEX composite: HSV protein (brown) restricted to necrotic regions with degraded DAPI and absent GFAP (red dotted line). Scale bars: 2 mm (a and b) and 200 µm (c–e).

(B) Fold enrichment of cell types near HSV$^+$ foci (0–50 µm, n = 9 tumors) (CODEX).

(C) Xenium detection of HSV (*ICP4*, *ICP22*, *ICP27*, *ICP34.5*, *gC*) in necrotic areas (red dotted line) of post-treatment samples. Red star indicates focal expression (see Figure S5B). Scale bars: 1 mm (left column) and 2.5 mm (right column).

(D) Distance to nearest HSV$^+$ region (defined as 20 HSV$^+$ cells). Low-count/necrotic cells were closest, and B cells, T cells, and plasma cells were most distant.

(E) Cell type composition across increasing distance intervals from HSV$^+$ regions.

(F) Xenium image showing macrophages/monocytes and neutrophils surrounding an HSV$^+$ region.

Scale bars: 500 µm.

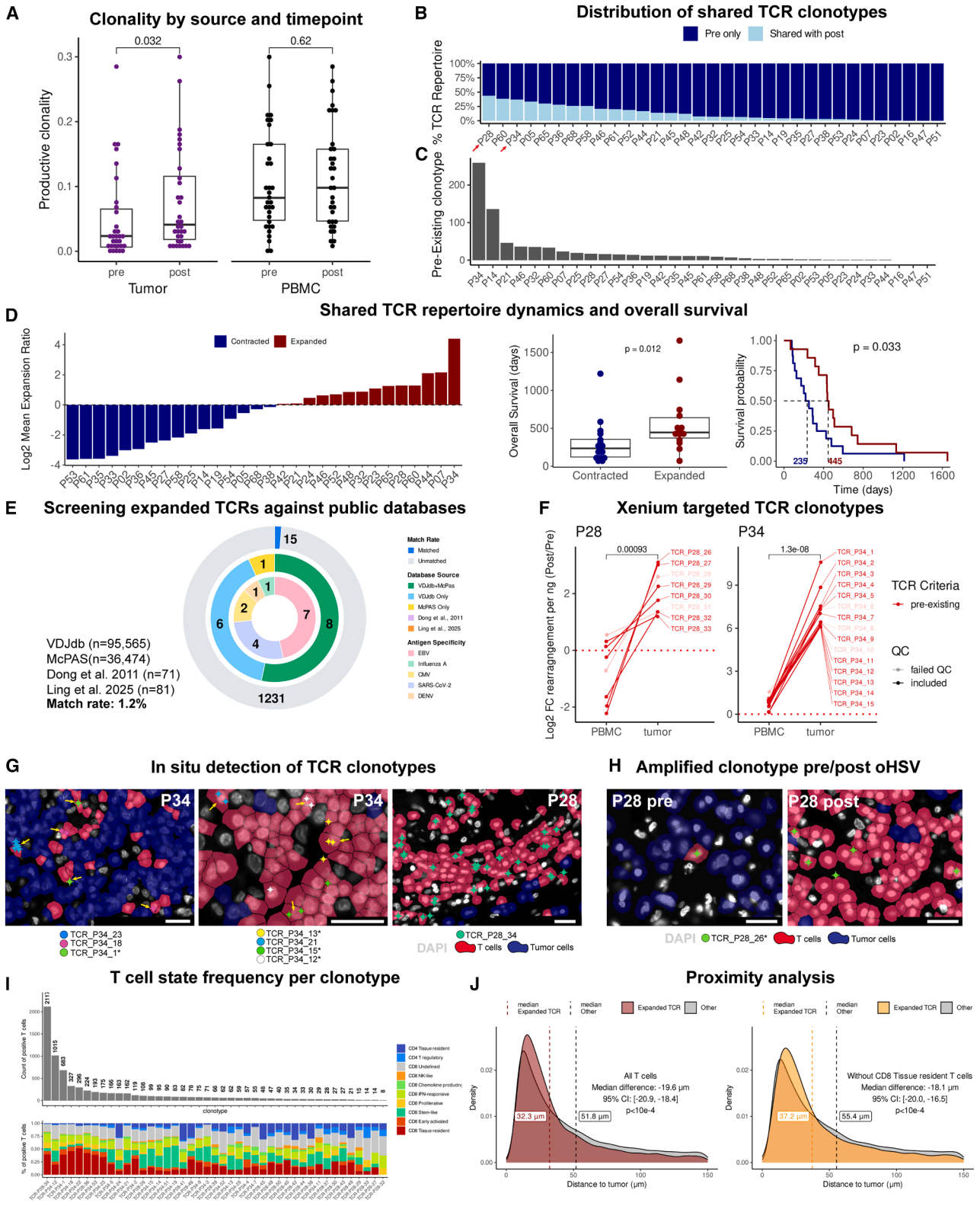

Figure 6. Expansion of TCR clonotypes and their spatial localization post-oHSV treatment

(A) Productive T cell clonality measured in tumor and PBMC pre- and post-treatment. Wilcoxon rank-sum *p* values are shown.

(B) Proportion of TCR clonotypes detected at both pre- and post-treatment tumor samples. Red arrows indicate patients selected for spatial TCR tracking.

(legend continued on next page)

(Figure 5E) showed enrichment of necrotic and tumor cells within 0–50 μm of HSV⁺ sites surrounded by macrophages/monocytes (Figure 5F), yet progressive enrichment of T cells at larger distances.

In the limited subset of HSV⁺ samples, concordant protein (IHC) and nucleic acid detection (Xenium) were restricted to necrotic, non-viable regions (Figures 5C, 5F, and S5C). It is possible that the Xenium probes detected residual viral DNA rather than RNA given the necrotic nature of these regions. This spatial segregation between T cells and residual HSV-containing areas indicates that viral antigen recognition is unlikely to represent the ongoing driver of deep T cell infiltration into live tumor areas at late time points following treatment.

Expansion of pre-existing tumor-infiltrating T cell clones by oHSV

To assess the specificity of ongoing T cell responses, we obtained bulk tumor and blood TCRβ chain (*TRBC*) sequencing from 33 pre- and post-oHSV patients.[11] We observed marked expansion of T cell clonotypes post-treatment, with prominent representation of highly expanded clones post-treatment in a subset of patients (Figure S6A). Notably, productive clonality significantly increased in post-oHSV tumor samples (p = 0.0320), while remaining stable in matched peripheral blood mononuclear cells (PBMCs; p = 0.62) (Figure 6A). To further investigate local amplification of the T cell response, we computed the fold change between pre- and post-treatment samples in tumor and PBMC compartments: tumor-infiltrating T cells underwent large shifts, reaching up to 1,024-fold higher inferred density, whereas PBMCs remained near baseline (Figure S6B), indicating a tumor-localized response. To investigate factors driving heterogeneous T cell responses, we examined the impact of dexamethasone, which is commonly used to control GBM-associated edema.[19] Treatment with dexamethasone for >100 days correlated with reduced T cell clonality following oHSV treatment (r = −0.414, p = 0.04), indicative of depletion of expanded clonotypes (Figure S6C). Therefore, dexamethasone exposure could significantly impair intratumoral T cell responses, consistent with previous studies in GBM.[3,20,21]

TCR repertoire analysis revealed that on average 13% of pre-oHSV clonotypes were also detected in post-treatment samples, with over 200 unique TCR clones for P34 (Figures 6B and 6C). We classified patients as having either "expanded" or "contracted" shared clonotype repertoires (Figure 6D, left). Patients whose shared clonotypes expanded post-treatment had longer survival than those with contracted repertoires (p = 0.012) (Figure 6D, middle), with median overall survival of 445 versus 235 days (p = 0.033) (Figure 6D, right).

To investigate whether expanded clonotypes were virus specific, we screened TCRβ chains against VDJdb[22] (n = 95,565) and McPAS-TCR[23] (n = 36,474), including T cells specific for HSV-1 (Ling et al.,[24] n = 81, including 50 oHSV-specific TCRs) and HSV-2 (Dong et al.,[25] n = 71). We selected clonotypes enriched at least 2-fold between pre- and post-treatment time points or counted at least 10 times in post-treatment samples. Only 15 of 1,246 clonotypes matched known specificities, mainly non-HSV viruses, and none matched HSV (Figure 6E). A tumor-reactive signature[26–28] (high expression of *CXCL13*, *ENTPD1*, *ZNF683*, and *ITGAE*; low expression of *IL7R* and *TCF7*) was enriched in T cells within 50 μm of tumor cells across all eight post-treatment samples (p = 0.0078) (Figure S7A), consistent with tumor reactivity at these later time points.

To spatially track shared T cell clonotypes *in situ*, we focused on two distinct categories of expanded T cell populations: "pre-existing clonotypes" (detected both pre- and post-oHSV) and "emergent clonotypes" (detected only post-oHSV, although potentially below the detection threshold in pre-treatment samples). For spatial mapping in our Xenium assay, we selected the most highly expanded clonotypes from both categories for two patients, P28 and P34, who demonstrated robust T cell responses and had among the highest proportion of shared TCR clonotypes between pre and post treatment (Figures 6B, red arrows, and S6D, red boxes). These patients also exhibited high T cell densities in the CODEX dataset, increasing the probability of detecting expanded clonotypes despite analysis of single 5 μm sections.

We targeted 35 clonotypes per patient. Using a ≥10 post-treatment template threshold, we selected 8 pre-existing and 27 emergent clonotypes for P28 and 15 pre-existing and 20 emergent for P34, and 43 of 70 passed probe QC for Xenium (Figure S6E). Clonal dynamics (Figure 6F) revealed a striking contrast between PBMC and tumor compartments: while most clonotypes showed modest expansion in PBMCs, they demonstrated dramatic enrichment in the tumor microenvironment, with log2FC values of >6 (64-fold) for some TCRs. All clonotypes were enriched in the tumor compartment compared with matched PBMCs (P28, p = 0.00093; P34, p = 1.3e−8), demonstrating that T cell expansion was predominantly localized within the tumor microenvironment rather than the systemic circulation.

(C) Number of unique TCR clonotypes shared between pre- and post-treatment tumor samples.
(D) Grouping of patients based on treatment-related expansion of pre-existing TCR clonotypes (left) and its correlation with overall survival (middle, boxplot with Wilcoxon rank-sum test; right, Kaplan-Meier analysis with log-rank test p).
(E) Multi-layered donut chart of TCRβ screening against TCR databases with annotated antigen specificity. Concentric rings show the match rate (outer), database source (middle), and antigen specificity (inner). Numbers indicate TCR counts per category.
(F) Log_2-fold enrichment of selected TCR clonotypes following treatment in PBMC and tumor for patients P28 and P34 (dotted line indicates absence of enrichment). Wilcoxon signed-rank p values are shown.
(G) *In situ* detection of expanded TCR clonotypes in post-treatment sections; * indicates pre-existing expanded TCRs. Scale bars: 25 μm.
(H) *In situ* detection of pre-existing clonotype TCR_P28_26 in both pre- and post-treatment samples of patient P28. Scale bars: 25 μm.
(I) Cell state distribution for each TCR clonotype, showing enrichment for the CD8 tissue-resident state.
(J) Spatial proximity of expanded versus non-expanded T cells to tumor cells, shown with and without filtering for CD8 tissue-resident T cells. Bootstrap estimated median differences and Wilcoxon rank-sum p values are shown.
See also Figure S6.

Xenium-based TCR mapping demonstrated high specificity and successful detection of expanded T cell clonotypes *in situ*. Examination of raw TCR counts (Figure S6F) revealed highly specific labeling, with TCR probes selectively detecting transcripts in the corresponding patient samples. Notably, control samples from other patients' samples showed no significant TCR detection. High-resolution imaging validated the specificity of our approach, showing TCR transcripts localized within T cells (Figure 6G, left), with some cells containing multiple copies of the same TCR transcript (Figure 6G, middle). Additionally, clonotypes were detected in multiple T cells, and TCR_P28_34 was detected in 1,985 T cells across the tissue (Figure 6G, right). Importantly, we could spatially track individual clones over time, as demonstrated by the pre-existing clone TCR_P28_26, which was successfully detected in both pre- and post-treatment samples (Figure 6H). Furthermore, approximately 77% of the TCR probes (33/43) showed robust detection in their target samples, with signals clearly distinguishable from the background.

The expanded TCR-labeled T cells showed distinct functional programs with high expression of tissue-residency genes (*ITGAE*/CD103 and *ZNF683*/HOBIT) and cytotoxic state (*PRF1* and *IFNG*). Many of the most expanded TCR clones had a prominent fraction of CD8 tissue-resident T cells, with some clones showing up to 50% enrichment of this T cell state (Figure 6I). To quantify this preferential distribution, we compared cell state enrichment across each targeted T cell clone (Figure 6I).

We reconstructed full-length TCRs from post-treatment single-cell RNA sequencing (scRNA-seq) of patient P28. Among clonotypes represented by at least four cells, more than half were expanded, whereas singletons were almost all non-expanded (Figure S6G). Expanded clones showed higher cytotoxicity and tissue-residency signatures than other T cells (p = 0.00079 and p = 0.0301) (Figure S6H).

Expanded T cell clonotypes were closer to tumor cells than other T cells (median 32.3 versus 51.8 μm) (Figure 6J, left), resulting in a significant median difference of −19.6 μm (95% CI: [−20.7, −18.4], p < 10e−4). This effect persisted even after excluding CD8 tissue-resident T cells (Figure 6J, right), with a comparable median difference of −18.1 μm (95% CI: [−20.0, −16.3], p < 10e−4), indicating that tumor proximity may reflect TCR specificity rather than residency alone. Thus, clonal expansion of T cells after oHSV was accompanied by tissue residency and effector phenotypes in tumor-infiltrating T cells.

Spatial mechanisms of therapy resistance

Despite enhanced T cell responses following oHSV treatment, not all patients demonstrated favorable clinical responses, suggesting the presence of tumor-intrinsic resistance mechanisms. We therefore characterized the molecular heterogeneity of tumor cells and their spatial relationship with infiltrating T cells. Using our custom Xenium panel, we classified tumor cells according to established GBM cell states (Figure 7A).[1] These six GBM cell states included neural-progenitor-cell-like populations (NPC-like 1 and 2), oligodendrocyte-progenitor-cell-like populations (OPC-like), AC-like cells, and two MES-like populations (MES-like 1 and MES-like 2, the latter characterized by a hypoxic signature). We validated our annotation through expression of canonical marker genes (Figure S7B). Across samples, all six GBM cell states were present with variable proportions (Figure S7C). Following oHSV treatment, we observed a striking redistribution of these cell states, with marked expansion of the hypoxic mesenchymal population (tumor MES-like 2) from pre-treatment to post-treatment samples at time of relapse (log2FC = 1.38, p = 0.00781) (Figures 7B and 7C).

To determine whether this hypoxic mesenchymal phenotype might contribute to treatment resistance, we analyzed the spatial relationship between tumor cells and infiltrating T cells. Differential gene expression analysis revealed that tumor cells most distant from T cells (top 80th percentile, ≥149 μm) exhibited significantly higher expression of hypoxia-related genes, including *CA9* and *VEGFA*, and core components of the MES-like 2 (hypoxia) signature (*ADM*, *DDIT3*, *ENO2*, and *HILPDA*) (Figure 7D). These genes displayed a progressive gradient of expression that correlated with increasing distance from T cells (Figure 7E). Interestingly, *VEGFA* was independently correlated with the MES-like 2 (hypoxia) gene signature (cor = 0.64, p < 1e–4). This gene had a robust expression and could be used as a single gene to identify hypoxic regions.

Classifying malignant cell states by T cell proximity revealed enrichment of the hypoxic MES-like 2 population in regions most distant from T cells (r = 0.457, p < 10e−4) (Figures 7E, 7F, S7D, and S7E). In the furthest regions (90–100th percentile: 214–3,456 μm), hypoxic MES-like cells constituted up to 78% of total tumor cells (Figures 7F and S7D). *VEGFA*-high hypoxic areas showed striking T cell exclusion despite infiltration in adjacent non-hypoxic regions (Figure 7G), suggesting a mechanism whereby hypoxic mesenchymal tumor regions inhibited T cell infiltration. Exclusion was independent of HSV status (Figure S7F) and *NES* (nestin) expression (Figure S7G). These findings indicate that T cell exclusion was likely driven by the hypoxic mesenchymal state rather than differential viral replication.

In summary, our spatial analysis revealed that despite robust T cell infiltration induced by oncolytic virus treatment, hypoxic mesenchymal regions may represent potential sites of resistance. These regions showed upregulation of key genes, including *VEGFA*, that correlated with increasing distance from T cells. This spatial organization suggests that hypoxic tumor microenvironments create zones of T cell exclusion, potentially contributing to heterogeneous treatment responses despite induction of anti-tumor T cell responses.

DISCUSSION

These data demonstrate that a single intratumoral oncolytic virus treatment can induce deep, persistent T cell infiltration in human GBM, including late time points (>6 months). Thus far, GBM has been refractory to efforts to develop immune interventions, in part because GBM is characterized by sparse T cell infiltration, with T cells primarily residing in perivascular spaces rather than infiltrating deeply into tumor areas.[2,29] Importantly, residual viral protein or nucleic acids were only detected in necrotic tumor regions, and a systematic distance analysis demonstrated that macrophages and neutrophils, but not T cells, were located close to such necrotic regions. Rather, T cell infiltration showed

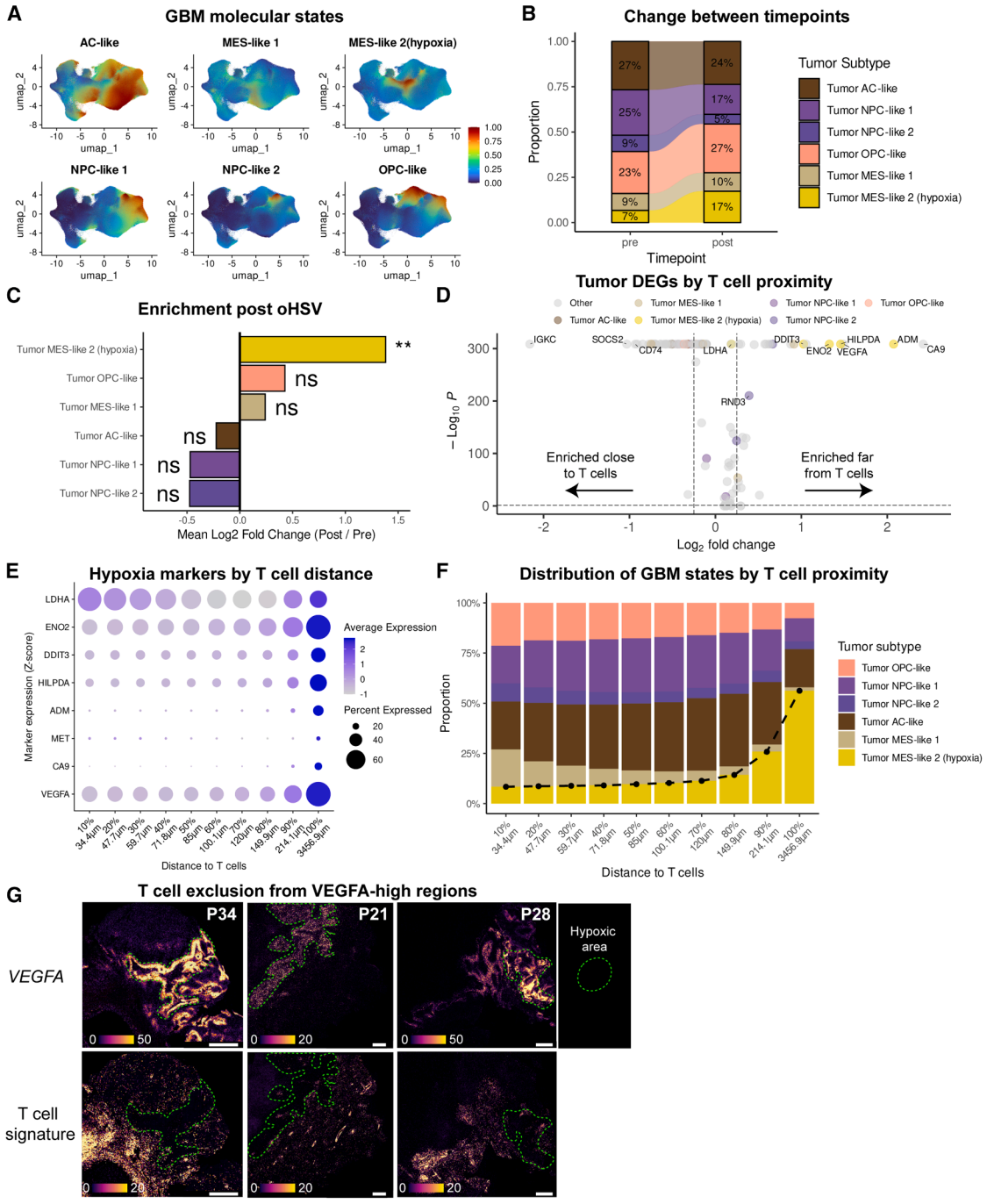

Figure 7. T cell exclusion from hypoxic mesenchymal tumor regions

(A) UMAP of tumor cell states from Xenium data in pre- and post-treatment samples.

(B) Average proportions of tumor cell states before and after treatment across pre- and post-treatment samples.

(C) Log_2 fold change for tumor cell states between pre- and post-treatment specimens. Log2 fold changes tested against zero using Wilcoxon signed-rank test.

(D) Volcano plot of differentially expressed genes in tumor cells distant from T cells (≥138 μm). Adjusted Wilcoxon rank-sum *p* values are shown.

(E) Dot plot showing expression of hypoxia-related genes in tumor cells according to distance to T cells.

(F) Tumor cell state proportions according to distance to T cells.

(G) Visualization of T cell exclusion by overlay of *VEGFA* expression (identifying hypoxic regions, green dotted line) and T cell signature (*CD2*, *CD3D*, *CD3E*, *CD8A*, *CD8B*, *GZMA*, and *GZMB*) in post-treatment tumors. Scale bars: 1 mm.

See also Figure S7.

a negative spatial correlation with such necrotic regions. This spatial distribution of T cell infiltration is inconsistent with the notion that sustained T cell infiltration into tumor regions is primarily driven by viral antigen recognition at these late time points.

We provide *in situ* evidence for T cell-mediated cytotoxicity in human GBM based on close physical proximity of GZMB$^+$ CD8 T cells with tumor cells undergoing caspase-3-mediated apoptosis (cl-Casp3$^+$), a sensitive marker of T cell killing validated *in vitro*.[30] Only GZMB-positive T cells spatially correlated with cl-Casp3$^+$ tumor cells, while GZMB$^-$ T cells showed the opposite pattern. It was surprising that such cytotoxicity events could be imaged *in situ* considering that apoptotic cells tend to be rapidly removed by macrophages, a cell type abundant in GBM.[31–33] Distance-based analysis showed that tumor-proximal CD8 T cells expressed higher levels of GZMB, PD-1, and CD44, consistent with cytotoxic activity. This spatial relationship between GZMB$^+$ CD8 T cells and apoptotic tumor cells may be clinically meaningful because it was associated with both slower tumor growth and longer PFS following virus injection. However, definitive proof of such T cell-mediated cytotoxicity would require *in vivo* live cell imaging.

Spatial transcriptomics analysis using the Xenium platform provided important evidence for an early activation program by T cells positioned close to tumor cells, including expression of *NR4A1*, *CD69*, *IFNG*, and *TNF*. We propose that this early T cell activation program is induced by TCR-mediated antigen recognition, most likely tumor antigens, given the large distances between such T cells and necrotic areas containing residual viral elements. T cells with such an early activation program represented a strongly enriched T cell state following treatment. Importantly, we also demonstrated that pre-existing tumor-infiltrating T cell clones were expanded by oncolytic virus treatment. Spatial tracking of such expanded TCRs based on unique CDR3-targeted probes documented close interactions of such clonally expanded pre-existing T cells with tumor cells. Clonal expansion by such pre-existing T cells was associated with a significant survival benefit and may therefore be clinically relevant. Together, these findings provide, to our knowledge, the first *in situ* evidence that oHSV amplifies pre-existing tumor-infiltrating T cells in human GBM that may recognize tumor antigens. This suggests an engineering path for next-generation vectors that include payloads designed to enhance the expansion and persistence of pre-existing GBM-infiltrating T cells, including IL-15 or 4-1BBL.

We propose that oncolytic virus treatment induces innate immune activation in GBM cells, for example, through the cGAS-STING pathway responsive to such a DNA virus,[34] leading to enhanced presentation of GBM tumor antigens via the MHC-I pathway to pre-existing tumor-reactive T cells. Oncolytic virus treatment, of course, also induces an anti-viral T cell response that may be prominent at early time points. However, we hypothesize that at late time points, tumor-reactive T cells represent a significant fraction of those cells that infiltrate deeply into the tumor and exhibit molecular programs of early T cell activation. These findings are consistent with the hypothesis that induction of T cell-mediated tumor immunity is a major mechanism accounting for the efficacy of oncolytic virus therapies.[35]

T cells are highly migratory cells, which complicates the analysis of their spatial interactions. We devised a novel approach to examine T cell molecular programs based on their distance to tumor cells. This revealed the large-scale organization of the response, with tissue-resident T cells infiltrating deeply into tumor regions while memory-like T cells were positioned in lymphoid clusters. Tumor-proximal T cells expressed key transcription factor *ZNF683* (HOBIT), the integrin *ITGAE* (CD103), and the cytotoxicity molecules *GZMA*, *GZMB*, and *PRF1*, consistent with the tissue-residency program.[24,36] These tissue-resident T cells also expressed the *CCR5* and *CCR1* chemokine receptors responsive to CCL4 and CCL5, suggesting a mechanism by which pioneer T cells recruit additional T cells into tumor regions.[18] At larger distances from tumor cells, T cells with a memory program (*TCF7*, *IL7R*, *SELL*, and *LTB*) were organized into lymphoid clusters with dendritic cells, B cells, and other immune cells. These T cells likely represent a reservoir of memory cells from which effector cells can be generated to sustain an anti-tumor response.

We also interrogated spatial mechanisms of resistance to oHSV. Our spatial data demonstrated striking exclusion of T cells from hypoxic regions, with a steep depletion gradient toward hypoxic, mesenchymal tumor regions. Hypoxia has long been recognized as a major organizing feature of GBM and as a mechanism of resistance to established therapies, including radiotherapy.[37–39] Also, prior work in other cancers has linked hypoxia to T cell exclusion and exhaustion.[40,41] These data suggest that hypoxia creates a gradient hindering T cell infiltration and/or causing T cell apoptosis, allowing tumor cells to adapt while escaping from T cell-mediated cytotoxicity. These results suggest combination therapies with oHSV, including PD-1-VEGF bispecific antibodies that have shown clinical activity in other cancer types.[42,43] VEGF blockade can also reduce brain edema, potentially enabling shorter dexamethasone exposure to preserve tumor-infiltrating T cells.[44] Complementing these observations, our data indicate that prolonged dexamethasone treatment significantly attenuates the therapeutic T cell response. Careful steroid management (minimizing dose and duration when clinically feasible) may therefore broaden the impact of oncolytic virus therapy.

Limitations of the study

This study was performed with tissue specimens from a phase 1 clinical trial with rQNestin34.5v.2. On-treatment biopsies at a defined time point would have been highly informative but are challenging to perform in GBM due to its intracranial localization. Our analysis therefore focused on surgical specimens at the time of recurrence. This approach afforded the unique opportunity to study the long-term impact of oncolytic virus treatment on T cell-mediated immunity. While the T cell response at early time points may be dominated by anti-viral T cells, such T cells may have limited impact on long-term tumor control once the virus has been contained. Given the cohort size (n = 16) and European-only ancestry, we could not assess demographic associations across ancestral backgrounds. Sex was balanced (8 females and 8 males), and prior trial analysis found no association between sex and outcome.[11] This study was not powered to detect sex-associated effects across the immunologic and spatial

endpoints. Unfortunately, no tumor cell lines were available from any of the patients for systematic testing of the anti-tumor activity of T cells with close interactions with tumor cells. Also, only TCRβ chain sequences were available from most patients. Systematic discovery of the antigen specificity of such T cells will require prospective tissue collection in a clinical trial to generate tumor cell lines against which TCRs identified by scRNA-seq can be tested for T cell-mediated cytotoxicity.

RESOURCE AVAILABILITY

Lead contact

Further information and requests for resources should be directed to the lead contact, Kai W. Wucherpfennig (kai_wucherpfennig@dfci.harvard.edu).

Materials availability

This study did not generate new, unique reagents.

Data and code availability

Raw and processed CODEX data are deposited in the EBI BioImage Archive: S-BIAD1921. Xenium data and processed Seurat objects are available through GEO: GSE296577. Code for CODEX image processing is available at https://github.com/DFCI-CODEX-group/CODEX-custom-pipeline, and full analysis workflows for CODEX and Xenium are available at https://github.com/maximemeylan/GBM_CAN3110.

ACKNOWLEDGMENTS

This work was supported by National Cancer Institute (NCI) grants P01 CA236749 (to K.W.W. and E.A.C.); P01 CA163222, R01 CA238039, and R01 CA251599 (to K.W.W.); and P01 CA163205 and R01 NS110942 (to E.A.C.). K.W.W. is a member of the Parker Institute for Cancer Immunotherapy (PICI) at Dana-Farber Cancer Institute. M.M. is a Cancer Research Institute Immuno-Informatics Fellow supported by the Cancer Research Institute (CRI award #CRI5000) and received mobility grants from l'Institut Servier (CT0101954) and the Philippe Foundation.

AUTHOR CONTRIBUTIONS

Conceptualization, K.W.W., E.A.C., M.M., and Y.T.; methodology, Y.T., M.M., S.M., and G.L.B.; investigation, M.M., Y.T., L. Wu, A.L.L., D.K., J.P., L.D.N., L. Westphal, J.M., L.N.G.C., S.D., and A.S.; visualization, M.M. and Y.T.; funding acquisition, K.W.W. and E.A.C.; project administration, K.W.W., E.A.C., and M.L.S.; supervision, K.W.W., E.A.C., M.L.S., and I.T.; writing – original draft, K.W.W., M.M., and Y.T.; writing – review & editing, K.W.W., E.A.C., M.L.S., I.T., M.M., Y.T., and A.L.L.

DECLARATION OF INTERESTS

K.W.W. serves on the scientific advisory boards of DEM BioPharma, Solu Therapeutics, D2M Biotherapeutics, DoriNano, Inc., and Nextechinvest; is a co-founder of Immunitas Therapeutics; receives sponsored research funding from Fate Therapeutics; and holds equity in TScan Therapeutics. These activities are not related to the research reported in this publication. M.L.S. is a scientific co-founder and advisory board member of Immunitas Therapeutics. E.A.C. is an advisor to Bionaut Labs, Seneca Therapeutics, Calidi Biotherapeutics, and RelgniteTherapeutics; has equity options in Bionaut Laboratories, RelgniteTherapeutics, Seneca Therapeutics, and Ternalys Therapeutics; and is co-founder and on the board of directors of Ternalys Therapeutics. Patents related to oHSV and CAN-3110 are under the possession of Brigham and Women's Hospital with E.A.C., and he is named as co-inventor. These patents have been licensed to Candel Therapeutics. Present and future milestone license fees and future royalty fees are distributed to Brigham and Women's Hospital from Candel.

STAR★METHODS

Detailed methods are provided in the online version of this paper and include the following:

- KEY RESOURCES TABLE
- EXPERIMENTAL MODEL AND STUDY PARTICIPANT DETAILS
  - Human subjects and clinical trial information
- METHOD DETAILS
  - CODEX Multiplexed Immunofluorescence
  - Xenium Spatial Transcriptomics
  - Xenium assay and imaging
  - Single-cell RNA-seq data generation
  - Single-cell RNA-seq data pre-processing
  - T Cell Receptor (TCR) Analysis
  - Spatial Analysis Methods
  - HSV Detection
- QUANTIFICATION AND STATISTICAL ANALYSIS
- ADDITIONAL RESOURCES
  - Xenium user guide

SUPPLEMENTAL INFORMATION

Supplemental information can be found online at https://doi.org/10.1016/j.cell.2025.12.055.

Received: May 13, 2025
Revised: October 23, 2025
Accepted: December 30, 2025
Published: February 11, 2026

REFERENCES

1. Neftel, C., Laffy, J., Filbin, M.G., Hara, T., Shore, M.E., Rahme, G.J., Richman, A.R., Silverbush, D., Shaw, M.L., Hebert, C.M., et al. (2019). An Integrative Model of Cellular States, Plasticity, and Genetics for Glioblastoma. Cell *178*, 835–849.e21. https://doi.org/10.1016/j.cell.2019.06.024.
2. Marx, S., Godicelj, A., and Wucherpfennig, K.W. (2022). A Conceptual Framework for Inducing T Cell-Mediated Immunity Against Glioblastoma. Semin. Immunopathol. *44*, 697–707. https://doi.org/10.1007/s00281-022-00945-5.
3. Mathewson, N.D., Ashenberg, O., Tirosh, I., Gritsch, S., Perez, E.M., Marx, S., Jerby-Arnon, L., Chanoch-Myers, R., Hara, T., Richman, A.R., et al. (2021). Inhibitory CD161 receptor identified in glioma-infiltrating T cells by single-cell analysis. Cell *184*, 1281–1298.e26. https://doi.org/10.1016/j.cell.2021.01.022.
4. Hara, T., Chanoch-Myers, R., Mathewson, N.D., Myskiw, C., Atta, L., Bussema, L., Eichhorn, S.W., Greenwald, A.C., Kinker, G.S., Rodman, C., et al. (2021). Interactions between cancer cells and immune cells drive transitions to mesenchymal-like states in glioblastoma. Cancer Cell *39*, 779–792.e11. https://doi.org/10.1016/j.ccell.2021.05.002.
5. Omuro, A., Brandes, A.A., Carpentier, A.F., Idbaih, A., Reardon, D.A., Cloughesy, T., Sumrall, A., Baehring, J., van den Bent, M., Bähr, O., et al. (2023). Radiotherapy combined with nivolumab or temozolomide for newly diagnosed glioblastoma with unmethylated MGMT promoter: An international randomized phase III trial. Neuro-oncology *25*, 123–134. https://doi.org/10.1093/neuonc/noac099.
6. Lim, M., Weller, M., Idbaih, A., Steinbach, J., Finocchiaro, G., Raval, R.R., Ansstas, G., Baehring, J., Taylor, J.W., Honnorat, J., et al. (2022). Phase III trial of chemoradiotherapy with temozolomide plus nivolumab or placebo for newly diagnosed glioblastoma with methylated MGMT promoter. Neuro-oncology *24*, 1935–1949. https://doi.org/10.1093/neuonc/noac116.
7. Reardon, D.A., Brandes, A.A., Omuro, A., Mulholland, P., Lim, M., Wick, A., Baehring, J., Ahluwalia, M.S., Roth, P., Bähr, O., et al. (2020). Effect of Nivolumab vs Bevacizumab in Patients With Recurrent Glioblastoma:

The CheckMate 143 Phase 3 Randomized Clinical Trial. JAMA Oncol. *6*, 1003–1010. https://doi.org/10.1001/jamaoncol.2020.1024.

8. Shalhout, S.Z., Miller, D.M., Emerick, K.S., and Kaufman, H.L. (2023). Therapy with oncolytic viruses: progress and challenges. Nat. Rev. Clin. Oncol. *20*, 160–177. https://doi.org/10.1038/s41571-022-00719-w.
9. Andtbacka, R.H.I., Kaufman, H.L., Collichio, F., Amatruda, T., Senzer, N., Chesney, J., Delman, K.A., Spitler, L.E., Puzanov, I., Agarwala, S.S., et al. (2015). Talimogene Laherparepvec Improves Durable Response Rate in Patients With Advanced Melanoma. J. Clin. Oncol. *33*, 2780–2788. https://doi.org/10.1200/JCO.2014.58.3377.
10. Todo, T., Ito, H., Ino, Y., Ohtsu, H., Ota, Y., Shibahara, J., and Tanaka, M. (2022). Intratumoral oncolytic herpes virus G47Δ for residual or recurrent glioblastoma: a phase 2 trial. Nat. Med. *28*, 1630–1639. https://doi.org/10.1038/s41591-022-01897-x.
11. Ling, A.L., Solomon, I.H., Landivar, A.M., Nakashima, H., Woods, J.K., Santos, A., Masud, N., Fell, G., Mo, X., Yilmaz, A.S., et al. (2023). Clinical trial links oncolytic immunoactivation to survival in glioblastoma. Nature *623*, 157–166. https://doi.org/10.1038/s41586-023-06623-2.
12. Goltsev, Y., Samusik, N., Kennedy-Darling, J., Bhate, S., Hale, M., Vazquez, G., Black, S., and Nolan, G.P. (2018). Deep Profiling of Mouse Splenic Architecture with CODEX Multiplexed Imaging. Cell *174*, 968–981.e15. https://doi.org/10.1016/j.cell.2018.07.010.
13. Janesick, A., Shelansky, R., Gottscho, A.D., Wagner, F., Williams, S.R., Rouault, M., Beliakoff, G., Morrison, C.A., Oliveira, M.F., Sicherman, J.T., et al. (2023). High resolution mapping of the tumor microenvironment using integrated single-cell, spatial and in situ analysis. Nat. Commun. *14*, 8353. https://doi.org/10.1038/s41467-023-43458-x.
14. Ashouri, J.F., and Weiss, A. (2017). Endogenous Nur77 Is a Specific Indicator of Antigen Receptor Signaling in Human T and B Cells. J. Immunol. *198*, 657–668. https://doi.org/10.4049/jimmunol.1601301.
15. Wykoff, C.C., Beasley, N.J., Watson, P.H., Turner, K.J., Pastorek, J., Sibtain, A., Wilson, G.D., Turley, H., Talks, K.L., Maxwell, P.H., et al. (2000). Hypoxia-inducible expression of tumor-associated carbonic anhydrases. Cancer Res. *60*, 7075–7083. https://pubmed.ncbi.nlm.nih.gov/11156414/.
16. Moran, A.E., Holzapfel, K.L., Xing, Y., Cunningham, N.R., Maltzman, J.S., Punt, J., and Hogquist, K.A. (2011). T cell receptor signal strength in Treg and iNKT cell development demonstrated by a novel fluorescent reporter mouse. J. Exp. Med. *208*, 1279–1289. https://doi.org/10.1084/jem.20110308.
17. Masopust, D., and Soerens, A.G. (2019). Tissue-Resident T Cells and Other Resident Leukocytes. Annu. Rev. Immunol. *37*, 521–546. https://doi.org/10.1146/annurev-immunol-042617-053214.
18. González-Martín, A., Gómez, L., Lustgarten, J., Mira, E., and Mañes, S. (2011). Maximal T cell-mediated antitumor responses rely upon CCR5 expression in both CD4(+) and CD8(+) T cells. Cancer Res. *71*, 5455–5466. https://doi.org/10.1158/0008-5472.CAN-11-1687.
19. Afshari, A.R., Sanati, M., Aminyavari, S., Shakeri, F., Bibak, B., Keshavarzi, Z., Soukhtanloo, M., Jalili-Nik, M., Sadeghi, M.M., Mollazadeh, H., et al. (2022). Advantages and drawbacks of dexamethasone in glioblastoma multiforme. Crit. Rev. Oncol. Hematol. *172*, 103625. https://doi.org/10.1016/j.critrevonc.2022.103625.
20. Keskin, D.B., Anandappa, A.J., Sun, J., Tirosh, I., Mathewson, N.D., Li, S., Oliveira, G., Giobbie-Hurder, A., Felt, K., Gjini, E., et al. (2019). Neoantigen vaccine generates intratumoral T cell responses in phase Ib glioblastoma trial. Nature *565*, 234–239. https://doi.org/10.1038/s41586-018-0792-9.
21. Iorgulescu, J.B., Gokhale, P.C., Speranza, M.C., Eschle, B.K., Poitras, M.J., Wilkens, M.K., Soroko, K.M., Chhoeu, C., Knott, A., Gao, Y., et al. (2021). Concurrent Dexamethasone Limits the Clinical Benefit of Immune Checkpoint Blockade in Glioblastoma. Clin. Cancer Res. *27*, 276–287. https://doi.org/10.1158/1078-0432.CCR-20-2291.
22. Shugay, M., Bagaev, D.V., Zvyagin, I.V., Vroomans, R.M., Crawford, J.C., Dolton, G., Komech, E.A., Sycheva, A.L., Koneva, A.E., Egorov, E.S., et al. (2018). VDJdb: a curated database of T-cell receptor sequences with known antigen specificity. Nucleic Acids Res. *46*, D419–D427. https://doi.org/10.1093/nar/gkx760.
23. Tickotsky, N., Sagiv, T., Prilusky, J., Shifrut, E., and Friedman, N. (2017). McPAS-TCR: a manually curated catalogue of pathology-associated T cell receptor sequences. Bioinformatics *33*, 2924–2929. https://doi.org/10.1093/bioinformatics/btx286.
24. Ling, A.L., Gantchev, J., Prabhu, M.C., Basu, S., Ahn, R., D'Souza, A., Masud, N., Ball, A., Nikas, O., Villa, G.R., et al. (2025). Serial multiomics uncovers anti-glioblastoma responses not evident by routine clinical analyses. Sci. Transl. Med. *17*, eadv2881. https://doi.org/10.1126/scitranslmed.adv2881.
25. Dong, L., Li, P., Oenema, T., McClurkan, C.L., and Koelle, D.M. (2010). Public TCR Use by Herpes Simplex Virus-2–Specific Human CD8 CTLs. J. Immunol. *184*, 3063–3071. https://doi.org/10.4049/jimmunol.0903622.
26. Oliveira, G., Stromhaug, K., Klaeger, S., Kula, T., Frederick, D.T., Le, P.M., Forman, J., Huang, T., Li, S., Zhang, W., et al. (2021). Phenotype, specificity and avidity of antitumour CD8+ T cells in melanoma. Nature *596*, 119–125. https://doi.org/10.1038/s41586-021-03704-y.
27. Hanada, K.I., Zhao, C., Gil-Hoyos, R., Gartner, J.J., Chow-Parmer, C., Lowery, F.J., Krishna, S., Prickett, T.D., Kivitz, S., Parkhurst, M.R., et al. (2022). A phenotypic signature that identifies neoantigen-reactive T cells in fresh human lung cancers. Cancer Cell *40*, 479–493.e6. https://doi.org/10.1016/j.ccell.2022.03.012.
28. Caushi, J.X., Zhang, J., Ji, Z., Vaghasia, A., Zhang, B., Hsiue, E.H.C., Mog, B.J., Hou, W., Justesen, S., Blosser, R., et al. (2021). Transcriptional programs of neoantigen-specific TIL in anti-PD-1-treated lung cancers. Nature *596*, 126–132. https://doi.org/10.1038/s41586-021-03752-4.
29. Woroniecka, K.I., Rhodin, K.E., Chongsathidkiet, P., Keith, K.A., and Fecci, P.E. (2018). T-cell Dysfunction in Glioblastoma: Applying a New Framework. Clin. Cancer Res. *24*, 3792–3802. https://doi.org/10.1158/1078-0432.CCR-18-0047.
30. He, L., Hakimi, J., Salha, D., Miron, I., Dunn, P., and Radvanyi, L. (2005). A sensitive flow cytometry-based cytotoxic T-lymphocyte assay through detection of cleaved caspase 3 in target cells. J. Immunol. Methods *304*, 43–59. https://doi.org/10.1016/j.jim.2005.06.005.
31. Parnaik, R., Raff, M.C., and Scholes, J. (2000). Differences between the clearance of apoptotic cells by professional and non-professional phagocytes. Curr. Biol. *10*, 857–860. https://doi.org/10.1016/s0960-9822(00)00598-4.
32. Arandjelovic, S., and Ravichandran, K.S. (2015). Phagocytosis of apoptotic cells in homeostasis. Nat. Immunol. *16*, 907–917. https://doi.org/10.1038/ni.3253.
33. Khan, F., Pang, L., Dunterman, M., Lesniak, M.S., Heimberger, A.B., and Chen, P. (2023). Macrophages and microglia in glioblastoma: heterogeneity, plasticity, and therapy. J. Clin. Investig. *133*, e163446. https://doi.org/10.1172/JCI163446.
34. Khoo, L.T., and Chen, L.Y. (2018). Role of the cGAS-STING pathway in cancer development and oncotherapeutic approaches. EMBO Rep. *19*, e46935. https://doi.org/10.15252/embr.201846935.
35. Russell, S.J., and Barber, G.N. (2018). Oncolytic Viruses as Antigen-Agnostic Cancer Vaccines. Cancer Cell *33*, 599–605. https://doi.org/10.1016/j.ccell.2018.03.011.
36. Zhao, Y., and Wucherpfennig, K.W. (2024). Tissue-Resident T Cells in Clinical Response and Immune-Related Adverse Events of Immune Checkpoint Blockade. Clin. Cancer Res. *30*, 5527–5534. https://doi.org/10.1158/1078-0432.CCR-23-3296.
37. Zheng, Y., Carrillo-Perez, F., Pizurica, M., Heiland, D.H., and Gevaert, O. (2023). Spatial cellular architecture predicts prognosis in glioblastoma. Nat. Commun. *14*, 4122. https://doi.org/10.1038/s41467-023-39933-0.
38. Greenwald, A.C., Darnell, N.G., Hoefflin, R., Simkin, D., Mount, C.W., Gonzalez Castro, L.N., Harnik, Y., Dumont, S., Hirsch, D., Nomura, M., et al. (2024). Integrative spatial analysis reveals a multi-layered organization of

glioblastoma. Cell *187*, 2485–2501.e26. https://doi.org/10.1016/j.cell.2024.03.029.

39. Chédeville, A.L., and Madureira, P.A. (2021). The Role of Hypoxia in Glioblastoma Radiotherapy Resistance. Cancers (Basel) *13*, 542. https://doi.org/10.3390/cancers13030542.
40. Scharping, N.E., Rivadeneira, D.B., Menk, A.V., Vignali, P.D.A., Ford, B.R., Rittenhouse, N.L., Peralta, R., Wang, Y., Wang, Y., DePeaux, K., et al. (2021). Mitochondrial stress induced by continuous stimulation under hypoxia rapidly drives T cell exhaustion. Nat. Immunol. *22*, 205–215. https://doi.org/10.1038/s41590-020-00834-9.
41. Wu, H., Zhao, X., Hochrein, S.M., Eckstein, M., Gubert, G.F., Knöpper, K., Mansilla, A.M., Öner, A., Doucet-Ladevèze, R., Schmitz, W., et al. (2023). Mitochondrial dysfunction promotes the transition of precursor to terminally exhausted T cells through HIF-1alpha-mediated glycolytic reprogramming. Nat. Commun. *14*, 6858. https://doi.org/10.1038/s41467-023-42634-3.
42. Fang, W., Zhao, Y., Luo, Y., Yang, R., Huang, Y., He, Z., Zhao, H., Li, M., Li, K., et al.; HARMONi-A Study Investigators (2024). Ivonescimab Plus Chemotherapy in Non-Small Cell Lung Cancer With EGFR Variant: A Randomized Clinical Trial. JAMA *332*, 561–570. https://doi.org/10.1001/jama.2024.10613.
43. Wang, L., Luo, Y., Ren, S., Zhang, Z., Xiong, A., Su, C., Zhou, J., Yu, X., Hu, Y., Zhang, X., et al. (2024). A Phase 1b Study of Ivonescimab, a Programmed Cell Death Protein-1 and Vascular Endothelial Growth Factor Bispecific Antibody, as First- or Second-Line Therapy for Advanced or Metastatic Immunotherapy-Naive NSCLC. J. Thorac. Oncol. *19*, 465–475. https://doi.org/10.1016/j.jtho.2023.10.014.
44. Banks, P.D., Lasocki, A., Lau, P.K.H., Sandhu, S., McArthur, G., and Shackleton, M. (2019). Bevacizumab as a steroid-sparing agent during immunotherapy for melanoma brain metastases: A case series. Health Sci. Rep. *2*, e115. https://doi.org/10.1002/hsr2.115.
45. Black, S., Phillips, D., Hickey, J.W., Kennedy-Darling, J., Venkataraaman, V.G., Samusik, N., Goltsev, Y., Schürch, C.M., and Nolan, G.P. (2021). CODEX multiplexed tissue imaging with DNA-conjugated antibodies. Nat. Protoc. *16*, 3802–3835. https://doi.org/10.1038/s41596-021-00556-8.
46. Schürch, C.M., Bhate, S.S., Barlow, G.L., Phillips, D.J., Noti, L., Zlobec, I., Chu, P., Black, S., Demeter, J., McIlwain, D.R., et al. (2020). Coordinated Cellular Neighborhoods Orchestrate Antitumoral Immunity at the Colorectal Cancer Invasive Front. Cell *183*, 838. https://doi.org/10.1016/j.cell.2020.10.021.
47. Kelly, S.T. (2023). Leiden: R implementation of the Leiden algorithm. https://cran.r-project.org/web/packages/leiden/leiden.pdf.
48. Melville, J. (2024). Uwot: The Uniform Manifold Approximation and Projection (UMAP) Method for Dimensionality Reduction (CRAN). https://cran.r-project.org/web/packages/uwot/index.html.
49. Barlow, G.L., Schürch, C.M., Bhate, S.S., Phillips, D.J., Young, A., Dong, S., Martinez, H.A., Kaber, G., Nagy, N., Ramachandran, S., et al. (2025). The extra-islet pancreas supports autoimmunity in human type 1 diabetes. eLife *13*, RP100535. https://doi.org/10.7554/eLife.100535.
50. Hao, Y., Stuart, T., Kowalski, M.H., Choudhary, S., Hoffman, P., Hartman, A., Srivastava, A., Molla, G., Madad, S., Fernandez-Granda, C., et al. (2024). Dictionary learning for integrative, multimodal and scalable single-cell analysis. Nat. Biotechnol. *42*, 293–304. https://doi.org/10.1038/s41587-023-01767-y.
51. Korsunsky, I., Millard, N., Fan, J., Slowikowski, K., Zhang, F., Wei, K., Baglaenko, Y., Brenner, M., Loh, P.R., and Raychaudhuri, S. (2019). Fast, sensitive and accurate integration of single-cell data with Harmony. Nat. Methods *16*, 1289–1296. https://doi.org/10.1038/s41592-019-0619-0.
52. Picelli, S., Faridani, O.R., Björklund, A.K., Winberg, G., Sagasser, S., and Sandberg, R. (2014). Full-length RNA-seq from single cells using Smart-seq2. Nat. Protoc. *9*, 171–181. https://doi.org/10.1038/nprot.2014.006.

STAR★METHODS

KEY RESOURCES TABLE

REAGENT or RESOURCE	SOURCE	IDENTIFIER
Antibodies		
Anti-human CD31, clone EP3095	Abcam	Cat# ab226157, RRID: AB_3094823
Anti-human CD4, clone EPR6855	Abcam	Cat# ab181724, RRID: AB_2864377
Anti-human HLA-DR, clone EPR3692	Abcam	Cat# ab209968, RRID: AB_3095318
Anti-human MHC-1, clone EMR8-5	Abcam	Cat# ab70328, RRID: AB_1269092
Anti-human CD3e, clone EP449E	Abcam	Cat# ab271850, RRID:AB_3698033
Anti-human CD163, clone EPR14643-36	Abcam	Cat# ab189915, RRID: AB_3493124
Anti-human CA9, clone M75	Absolute Antibody	Cat# Ab00414-1.4, RRID:AB_3717831
Anti-HSV1, polyclonal	Agilent Dako	Cat# B0114, RRID: AB_2732870
Anti-human CD20, clone H1	BD Bioscience	Cat# 555677, RRID: AB_396030
Anti-human Ki67, clone B56	BD Bioscience	Cat# 556003, RRID: AB_396287
Anti-human CD44, clone IM7	Biolegend	Cat# 103001, RRID: AB_312952
Anti-human Podoplanin, clone NC-08	Biolegend	Cat# 337002, RRID: AB_1595511
Anti-human CD66b, clone G10F5	BioLegend	Cat# 305102, RRID: AB_314494
Anti-human CD8, clone C8/144B	Biolegend	Cat# 372902, RRID: AB_2650657
Anti-human CD25, clone 4C9	Cell Marque	Cat# 125M-14, RRID: AB_1157925
Anti-human CD56, clone MRQ-42	Cell Marque	Cat# 156R-94, RRID:AB_2941091
Anti-human CD68, clone D4B9C	Cell Signaling Technology	Cat# 26042, RRID: AB_2920587
Anti-human PDL1, clone E1L3N	Cell Signaling Technology	Cat# 85164, RRID: AB_2922774
Anti-human CD133, clone D2V8Q	Cell Signaling Technology	Cat# 51917SF, RRID:AB_3717833
Anti-human PD-1, clone D4W2J	Cell Signaling Technology	Cat# 63815, RRID: AB_3675993
Anti-human GZMB, clone D6E9W	Cell Signaling Technology	Cat# 79903, RRID: AB_3665532
Anti-human cl.Casp3, clone D3E9	Cell Signaling Technology	Cat# 74860, RRID: AB_3679063
Anti-human CD24, clone SN3	MilliporeSigma	Cat# CBL561, RRID: AB_2072851
Anti-human CD45, clone 2B11 + PD7/26	Novus biologicals	Cat# NBP2-34528-0.1 mg, RRID: AB_2864384
Anti-human DC-LAMP, clone 1010E1.01	Novus biologicals	Cat# DDX0191P-100, RRID: AB_2827532
Anti-human CLEC2D, clone 2F1	This paper	N/A
Anti-human GFAP, clone GA5	Thermo Fisher Scientific	Cat# 14-9892-82, RRID: AB_10598206
Anti-human FOXP3, clone 236A/E7	Thermo Fisher Scientific	Cat# 14-4777-82, RRID: AB_467556
Biological samples		
Paraffin-embedded formalin fixed human GBM tumor slides, prepared from tumor resections	Dana-Farber Cancer Institute/Brigham and Women's Hospital	IRB# DF/HCC 16-557
Chemicals, peptides, and recombinant proteins		
CODEX barcode BX-001	Akoya Biosciences	Cat# 5450018
CODEX barcode BX-003	Akoya Biosciences	Cat# 5550017
CODEX barcode BX-005	Akoya Biosciences	Cat# 5450024
CODEX barcode BX-007	Akoya Biosciences	Cat# 5450020
CODEX barcode BX-010	Akoya Biosciences	Cat# 5450021
CODEX barcode BX-013	Akoya Biosciences	Cat# 5450022
CODEX barcode BX-015	Akoya Biosciences	Cat# 5550008
CODEX barcode BX-020	Akoya Biosciences	Cat# 5250002
CODEX barcode BX-021	Akoya Biosciences	Cat# 5550009
CODEX barcode BX-022	Akoya Biosciences	Cat# 5450003

(*Continued on next page*)

Continued

REAGENT or RESOURCE	SOURCE	IDENTIFIER
CODEX barcode BX-023	Akoya Biosciences	Cat# 5250003
CODEX barcode BX-025	Akoya Biosciences	Cat# 5450004
CODEX barcode BX-026	Akoya Biosciences	Cat# 5250004
CODEX barcode BX-027	Akoya Biosciences	Cat# 5550011
CODEX barcode BX-029	Akoya Biosciences	Cat# 5250005
CODEX barcode BX-031	Akoya Biosciences	Cat# 5450006
CODEX barcode BX-032	Akoya Biosciences	Cat# 5250006
CODEX barcode BX-033	Akoya Biosciences	Cat# 5550013
CODEX barcode BX-035	Akoya Biosciences	Cat# 5250007
CODEX barcode BX-036	Akoya Biosciences	Cat# 5550014
CODEX barcode BX-037	Akoya Biosciences	Cat# 5450008
CODEX barcode BX-040	Akoya Biosciences	Cat# 5450009
CODEX barcode BX-042	Akoya Biosciences	Cat# 5550015
CODEX barcode BX-045	Akoya Biosciences	Cat# 5550016
CODEX barcode BX-047	Akoya Biosciences	Cat# 5250009
CODEX barcode BX-049	Akoya Biosciences	Cat# 5450012
CODEX barcode BX-054	Akoya Biosciences	Cat# 5250010
CODEX Assay Reagent	Akoya Biosciences	Cat# 7000002
10X CODEX Buffer	Akoya Biosciences	Cat# 7000001
CODEX Storage Buffer	Akoya Biosciences	Cat# 232107
CODEX Nuclear Stain	Akoya Biosciences	Cat# 7000003
HistoChoice Clearing Agent	Millipore Sigma	Cat# H2779-1L
16% Paraformaldehyde	Electron Microscopy Sciences	Cat# 15710
1X PBS, pH7.2	Gibco, Thermo Fisher Scientific	Cat# 20012-027
Poly-L-lysine 0.1%	Sigma-Aldrich	Cat# P8920
DMSO - ACS reagent, ≥99.9%	Sigma-Aldrich	Cat# 472301-4L
Critical commercial assays		
CODEX Conjugation Kit	Akoya Biosciences	Cat# 7000009
CODEX Staining Kit	Akoya Biosciences	Cat# 7000008
Xenium Human Immuno-Oncology Profiling Panel	10X Genomics	Cat# 1000654
Xenium Decoding Consumables	10X Genomics	Cat# 1000487
Xenium Slides & Sample Prep Reagents	10X Genomics	Cat# 1000460
Xenium Decoding Reagents	10X Genomics	Cat# 1000461
Xenium Add-on Custom 51 to 100 Gene Panel Design ID# PKK3C7	10X Genomics	Cat# 1000651
Xenium Add-on Custom 1 to 50 Gene Panel	10x Genomics	Cat# 1000652
Xenium Add-on Custom 51 to 100 Gene Panel	10x Genomics	Cat# 1000651
Deposited data		
CODEX data	EBI BioImage Archive	https://www.ebi.ac.uk/biostudies/bioimages/studies/S-BIAD1921
Xenium data	NCBI GEO repository	https://www.ncbi.nlm.nih.gov/geo/query/acc.cgi?acc=GSE296577
Software and algorithms		
CODEX Instrument manager V1.30.0.12	Akoya Biosciences	https://help.codex.bio/codex/cim/
CODEX Processor V1.8.2.13	Akoya Biosciences	https://help.codex.bio/codex/processor/
ZEN V2.6	Carl Zeiss Microscopy GmbH	https://www.zeiss.com/microscopy/us/products/software/zeiss-zen.html
Biorender	Biorender	https://www.biorender.com

(*Continued on next page*)

Continued

REAGENT or RESOURCE	SOURCE	IDENTIFIER
CODEX data pre-processing	this paper	https://github.com/DFCI-CODEX-group/CODEX-custom-pipeline
Xenium and CODEX data analysis and figure generation	this paper	https://github.com/maximemeylan/GBM_CAN3110
R	https://www.r-project.org/	version 4.4.2
Leiden	https://github.com/TomKellyGenetics/leiden	version 0.4.3.1
Uwot	https://CRAN.R-project.org/package=uwot	version 0.2.2
Seurat	https://satijalab.org/seurat/	version 5.0.2
Harmony	https://github.com/immunogenomics/harmony	version 1.2.3
Other		
CODEX User Manual Rev_C	Akoya Biosciences	https://www.akoyabio.com/wp-content/uploads/2021/01/CODEX-User-Manual.pdf
CODEX Instrument	Akoya Biosciences	Cat# INST3000U
Microscope Axio Observer 7 KMAT	Carl Zeiss Microscopy GmbH	Product ID# 491915-9880-010
Photometrics Prime BSI sCMOS	Carl Zeiss Microscopy GmbH	Product ID# 410825-1035-000
Light Source Colibri 7 FR-R[G/Y]BV-UV	Carl Zeiss Microscopy GmbH	Product ID# 423052-9770-000
Xenium In Situ for FFPE - Tissue Preparation	10x genomics	CG000578 revF
Xenium In Situ Gene Expression - Probe Hybridization, Ligation & Amplification	10x genomics	CG000582 RevH

EXPERIMENTAL MODEL AND STUDY PARTICIPANT DETAILS

Human subjects and clinical trial information

Tumor samples were obtained from 16 patients with recurrent glioblastoma (rGBM) who were treated with a single intratumoral injection of rQNestin34.5v.2, an oncolytic herpes simplex virus (oHSV) in which the viral *ICP34.5* neurovirulence gene was placed under the transcriptional control of the nestin promoter. Paired pre-treatment biopsies and post-treatment resection specimens were collected from patients as part of a phase I clinical trial (NCT03152318). The cohort comprised patients aged 27–65 years (8 female, 8 male) treated at their first to fourth recurrence, with baseline KPS scores of 70–100. IDH-mutant disease was present in 5 of 16 patients, and 8 of 16 were HSV-1 seropositive prior to treatment. Clinical information including time to progression, overall survival, and steroid (dexamethasone) administration were obtained from Ling et al.[11] All patients were of European ancestry. This phase 1 clinical trial was approved by the National Institutes of Health (NIH) Recombinant DNA Advisory Committee (RAC) Office of Biotechnology Affairs (NIH no 1104-1100), the Dana Farber Harvard Comprehensive Cancer Center Institutional Review Board (IRB) (no 16-557). It was sponsored under Investigational New Drug (IND) no. 16380 (Dr. E. A. Chiocca, Brigham and Women's Hospital, Boston, MA).

METHOD DETAILS

CODEX Multiplexed Immunofluorescence

Patient GBM Tissue Processing

Paired pre- and post-treatment tumor FFPE blocks from 16 rGBM patients with reasonable tissue size and morphological quality were selected for CODEX multiplexed immunofluorescence experiments. For each FFPE block, a 5μm section was collected on a prepared 22μm x 22μm poly-L-lysine coated coverslip for CODEX analysis. For each post-treatment FFPE block, an additional 5μm section consecutive to the CODEX section was collected on the regular slide for performing immunohistochemistry for oHSV.

CODEX Antibody Panel Design

The fundamental principles of CODEX multiplex imaging and the general strategies for experimental design on human FFPE tissue have been described before[45,46]. Basically, CODEX (CO-Detection by indEXing) multiplexed imaging is a highly multiplexed fluorescence imaging platform that enables simultaneous detection of dozens of protein markers on a single tissue section while preserving

spatial resolution. In this approach, primary antibodies are conjugated to unique DNA oligonucleotide barcodes rather than fluorophores. All barcoded antibodies are applied to the tissue in a single staining step, allowing concurrent binding to their respective targets. Following antibody staining, iterative cycles of imaging are performed. In each cycle, a subset of complementary fluorescently labeled oligonucleotides is hybridized to the corresponding DNA barcodes, visualized by fluorescence microscopy, and subsequently removed through chemical stripping. This cyclic process enables multiplexed detection of a large number of protein targets using a limited number of fluorescence channels. Nuclear counterstaining is included in each cycle to facilitate image registration across imaging rounds. After image acquisition, individual imaging cycles are computationally aligned and combined to generate a high-dimensional spatial protein expression dataset. The resulting images retain subcellular resolution and enable quantitative analysis of cell phenotypes, spatial organization, and cell-cell interactions within the tissue microenvironment.

In the present study, a 27-protein marker CODEX panel was designed to enable comprehensive phenotyping of the tumor microenvironment. The panel included markers for T cells (CD3e, CD4, CD8, PD-1, GZMB, CD25, FOXP3), other immune cell populations (CD45, CD20, DC-LAMP, CD56, CD66b, CD68, CD163), stromal cells (CD31), GBM tumor cells (GFAP, CD44, CD133, CD24, Podoplanin), and functional cell states (MHC-I, HLA-DR, PD-L1, CLEC2D, CA9, Ki67, cleaved-Caspase 3) (Table S1). Each antibody was conjugated with a unique Akoya CODEX barcode by the CODEX Conjugation Kit (Akoya Biosciences, Cat# 7000009) following Akoya CODEX User Manual Rev_C Chapter 4. The full details of antibodies and their conjugated Akoya CODEX barcodes are listed in Table S2. All conjugated antibodies were validated before use in the present study.

CODEX Antibody Staining

CODEX antibody staining was performed from 16 patients on 21 regions for the pre-treatment samples and 28 regions for post-treatment using CODEX Staining Kit (Akoya Biosciences, Cat# 7000008). The staining steps followed the Akoya CODEX User Manual Rev_C Chapter 5, with optimization for the following aspects: 1. Following antigen retrieval, sections were placed in 5 ml Bleaching Buffer (4.5% H_2O_2 and 20 mM NaOH in PBS) in a 6-well plate with a lid. Two LED light pads were placed both below and above the 6-well plate to expose samples to the LED light for 45 minutes. The samples were then washed with PBS three times and equilibrated in Akoya CODEX Staining Buffer. 2. Before addition of CODEX antibody cocktail to samples, 190 μl CODEX Blocking Buffer was applied to each sample (1 hour incubation at room temperature). After the CODEX antibody staining was completed, all stained samples were stored at 4°C and imaged within one week.

CODEX Image Data Acquisition and Processing

CODEX imaging was performed on a custom platform connecting the Akoya CODEX Instrument with a Zeiss Axio Observer 7 widefield microscope equipped with a Colibri 7 Multicolor LED light source and a PRIME BSI high-resolution camera. All 27 CODEX markers were arranged into a 12-cycle imaging program, in which the first and last cycles were blank for background subtraction. The CODEX Reporter Plate corresponding to the 12-cycle program was prepared following Akoya CODEX User Manual Rev_C Chapter 7 and applied to the Akoya CODEX Instrument. The CODEX Instrument was set up with CODEX Instrument Manager version 1.30.0.12 following Akoya CODEX User Manual Rev_C Chapter 8, then the sample was loaded onto Zeiss microscope stage. The entire section was scanned using the DAPI channel to assess its location, size, and morphology, and large imaging regions were selected (two per section when feasible, totaling 28 regions scanned). The 12-cycle imaging program was then performed. For each imaging cycle, four fluorescent channels (DAPI, ATTO550, AF647, and AF750), 20x objective magnification, 5-layer multi-Z-stack scanning, and focus map supported by Zeiss Definite Focus 2 module were applied through Zeiss ZEN software.

The raw image data were acquired in CZI format, transferred using CODEX Instrument Manager and processed using CODEX Processor version 1.8.2.13. Deconvolution, background subtraction, extended depth of field, shading correction, and cycle alignment were applied. Processed and stitched images of entire imaged regions were generated. Then, whole cell segmentation was performed using DAPI (nuclear) and MHC-I (membrane) expression using a custom pipeline. Marker expression was quantified for each segmented cell. In total, 3.6 million cells were analyzed across all samples (https://github.com/DFCI-CODEX-group/CODEX-custom-pipeline).

Cell Type Annotation and Clustering

Cell clustering and annotation were performed through a multi-step process on the post treatment samples. First, marker expression values were normalized to account for background and technical variation across samples. UMAP dimensionality reduction was then applied to these normalized expression values using a set of structural markers to distinguish key cell populations: T cells (CD3ε, CD4, CD8), regulatory T cells (FOXP3, CD25), B cells (CD20), myeloid cells (CD68, CD163), neutrophils (CD66b), NK cells (CD45, CD56), antigen-presenting cells (HLA-DR, DC-LAMP), vessels (CD31), and tumor cells (GFAP, CD133, CD44, CD24). Blank channels were used to identify autofluorescent cells. Leiden clustering[47] was applied on the UMAP nearest-neighbor graph which identified 56 clusters which were annotated into 11 distinct cell clusters based on expression patterns of lineage-defining markers. UMAP and clustering were performed on a subset of the data (30% of the total cell count) and projected to the full dataset via the function umap_transform from the uwot R package.[48] Finally, cell annotations were manually finetuned using thresholds (DC-Lamp, B cells) or neural networked based methods.[49] Pre-treatment samples were annotated using XGBoost, a gradient boosting classifier trained on the annotated post-treatment dataset. The reference dataset was balanced by sampling up to 10,000 cells per cell type, and a stratified 80/20 train-validation split was used with early stopping to prevent overfitting. The model was trained on z-scored expression values of 20 structural markers (DAPI, CD45, CD3ε, CD4, FOXP3, CD8, CD25, DC-LAMP, HLA-DR, CD20, CD31, CD68, CD163, CD66b, CD56, GFAP, CD133, CD44, Blank-1, Blank-3) to predict cell type labels, achieving optimal performance after early stopping. Predicted annotations were manually refined using marker-based thresholds to correct misclassifications, particularly for dendritic

cells, B cells, and T cell subsets based on CD45, CD3ε, and lineage marker expression. Full code for pre-processing and figures available on github (github.com/maximemeylan/GBM_CAN3110).

CODEX data Availability

Comprehensive raw and processed CODEX data are deposited at EBI's BioImage archive repository under accession number BioImage: S-BIAD1921.

Xenium Spatial Transcriptomics

Probe Panel Design

The 10X Genomics Xenium spatial transcriptomics platform was used to analyze 8 matched pre- and post-oHSV treatment pairs (16 samples total). The commercial 380-gene immuno-oncology panel was used with an additional 100 custom probes targeting early T cell activation markers (including *NR4A1* and *CD69*), expanded TCR clonotypes identified in pre- and/or post-oHSV samples, GBM molecular state genes, and key HSV viral genes (*ICP4*, *ICP22*, *ICP27*, *ICP34.5*, *gC*). The 100-gene add-on panel (Design ID: PKK3C7) was designed with 10x Genomics using a human brain GBM single cell reference and included custom targets (viral HSV sequences and patients specific TCR CDR3 clonotypes). 8 probes per target were designed for non-TCR custom genes. For each TCR clonotype a single probe was used, clonotype-specific nucleotide sequences were centered on the CDR3 region with extended flanking sequences on V and J genes (16 to 18 bp on each side) to support probe placement across validated ligation junctions and maximize specificity. Probes were screened for potential cross-hybridization and cross-ligation across the entire panel. Targets with low predicted performance (design score <0.5) or lacking validated ligation junctions were removed. For a small number of clonotypes, probes could not be designed due to unfavorable sequence composition (GC-rich or repetitive motifs), consistent with manufacturer probe-design constraints. Final gene lists and custom target sequences were finalized prior to manufacturing (custom panel summary and design files provided in GEO entry GSE296577).

Patient GBM Tissue Selection and Processing

To perform 10X Genomics Xenium, paired pre- and post-treatment tumor FFPE blocks from 8 rGBM patients were selected based on morphological tissue quality and T cell infiltration, which were considered more likely to capture sufficient spatial and molecular features of T cells. For each selected FFPE block, a 5μm section was collected onto the Sample Area of 10X Genomics Xenium slides in an RNAse-free working environment.

Xenium assay and imaging

Sections were processed using the Xenium Prime In Situ Gene Expression workflow (10x Genomics) according to the manufacturer's instructions. Slides were baked at 60 °C for 2 hours, deparaffinized, followed by decrosslinking. The 380-gene Immuno-Oncology panel plus 100 custom probes were hybridized to tissue sections, followed by probe ligation, rolling-circle amplification, and iterative fluorescent reporter hybridization. Before transcript imaging, a whole-slide morphology pre-scan was performed to capture overall tissue layout and guide field-of-view (FOV) selection. FOVs containing tissue were manually selected on the Xenium Analyzer for spatial transcript acquisition. No data were acquired from FOVs lacking tissue, these regions therefore appear empty/black in the exported images and downstream analyses. Morphology pre-scan images and FOV selection for each sample are included in the deposited Xenium dataset at GEO: GSE296577. Nuclei were identified based on the DAPI channel and used for cell segmentation using the Xenium cell segmentation pipeline (default parameters, version 2.0.1.0). Cell boundaries were inferred by heuristic expansion of nucleus boundaries by 5 μm in X-Y until they hit another boundary. Transcripts were assigned to segmented cells based on their spatial coordinates relative to these inferred boundaries.

Data Preprocessing and Cell Type Annotation

Spatial transcriptomics was performed using the 10X Genomics Xenium platform. Cell segmentation was performed using the manufacturer's pipeline and data were further processed using a custom R workflow with Seurat.[50] Low-quality cells with fewer than 50 UMIs or 25 detected genes were removed and data from individual regions were merged. After filtering, a total of 2,401,946 cells were retained for downstream analysis, with a median of 182 transcripts and 68 genes detected per cell across all samples. Pre-treatment samples contributed 184,048 cells (median 143 UMIs and 59 genes per cell), and post-treatment samples contributed 2,217,898 cells (median 186 UMIs and 68 genes per cell).

Log-normalized gene expression data was dimensionally reduced using principal component analysis, excluding TCR and HSV-specific transcripts. TCR and HSV transcripts were retained for targeted analyses and visualization but excluded from PCA/Harmony to prevent sparse clonotype/viral features from driving global embeddings. Batch effects between samples were corrected using Harmony integration.[51] UMAP visualization was generated from the integrated embeddings, and a shared nearest-neighbor graph was constructed for community detection. Leiden clustering was applied to identify distinct cell populations.

Cell types were annotated using a two-tiered approach. First, major cell populations were identified based on canonical marker expression, including T cells (*CD3E*, *CD3D*, *CD8A*), NK cells (*KLRD1*, *NKG7*, *RUNX3*), B cells (*MS4A1*, *BANK1*, *TNFRSF13C*), plasma cells (*XBP1*, *SDC1*, *MZB1*), dendritic cells (*ITGAX*, *CD1C*, *LAMP3*), macrophages (*CD68*, *CD163*, *CSF1R*), neutrophils (*S100A9*, *ITGAM*), vasculature (*PLVAP*, *FLT1*, *NOTCH3*), stromal cells (*MGP*, *FN1*, *LUM*), and tumor cells (*GFAP*, *EGFR*, *SOX2*). This general set of annotations was defined as tier-1. More refined annotations were then applied to define tumor molecular subtypes (NPC-like, OPC-like, AC-like, MES-like and MES-like with hypoxia) based on established GBM subtype[1] markers and were referenced as tier-2 annotations.

For T cell-specific analyses, T cells were selected based on tier-1 annotations and clustered using the Harmony-corrected PCA approach while excluding potential contaminating genes from other cell types. T cell subclusters were annotated into functional states including tissue-resident (*ZNF683*, *ITGAE*), early activated (*NR4A1*, *CD69*, *IFNG*), stem-like (*IL7R*, *TCF7*, *SELL*), proliferative (*MKI67*, *CDK1*), IFN-responsive (*IFIT3*, *ISG15*), chemokine-producing (*CXCL1*, *CCL2*), NK-like (*GNLY*, *KLRC1*), regulatory (*FOXP3*, *CTLA4*), and CD4 tissue-resident (CXCR6, *KLRB1*, *CD40LG*) T cells. (Full code will be available as described above).

Tumor-reactive signature scoring

For each Xenium T cell, we computed a tumor-reactive score as mean(*CXCL13, ENTPD1, ZNF683, ITGAE*) minus mean(*IL7R*, TCF7) from normalized expression. T cell to tumor distance was obtained as described in the methods section labeled "Proximity analysis", T cells were classified as tumor-proximal <50 μm or tumor-distal ≥50 μm and scores were averaged per sample. Proximal versus distal means were compared across the eight post-treatment samples using a paired Wilcoxon test.

Xenium data availability

Full output from Xenium spatial transcriptomic assays and complete processed Seurat object available at NCBI's Gene Expression Omnibus (GEO) accession number GEO: GSE296577. Full code for pre-processing and figures available on github (github.com/maximemeylan/GBM_CAN3110).

Single-cell RNA-seq data generation

Fresh tumor was collected at the time of surgery and presence of glioblastoma was confirmed by frozen section. Tumor was mechanically and enzymatically dissociated using a papain-based tumor dissociation kit (Miltenyi Biotec). Tumor cells were blocked in 1% bovine serum albumin in Hanks buffered saline solution (BSA / HBSS). Tumors were first stained first with CD45 Vioblue (clone REA747, Miltenyi Biotec) and CD3 PE (clone BW264/56, Miltenyi Biotec) direct antibody conjugates for 30 min at 4° C. Cells were washed with cold PBS, and then re- suspended in 1mL of BSA / HBSS containing 1 mM Calcein AM (Life Technologies) and 0.33 mM TO-PRO-3 iodide (Life Technologies) to co-stain for 30 min before sorting. Live, single T cells (gating: Calcein AM+, TO-PRO-3-, CD45+, CD3+) were sorted into individual wells of a 96-well twin.tec PCR plate (Eppendorf; Hamburg, Germany) that contained 10μL/well of RTL buffer (Qiagen; Venlo, Netherlands), using a BD Biosciences Aria III fluorescence-activated cell sorter (FACS) with a 70μM nozzle. Plates were immediately centrifuged at 800 x *g* for 1 minute at 4°C and frozen on dry ice prior to whole transcriptome amplification, library preparation and sequencing. Smart-seq2 whole transcriptome amplification, library construction, and sequencing were performed as previously published[1,52]

Single-cell RNA-seq data pre-processing

The following preprocessing steps were performed before conducting downstream analysis: Cell filtering: We excluded cells with a low number of detected genes (#genes), using a cutoff of #genes > 1000. Gene filtering: Given an expression matrix A with n genes (rows) and m cells (columns), the mean expression of gene i across cells is given by $E_{i\ \{1..n\}} = \sum_{j=1}^{m} \frac{A_{ij}}{m}$. For most analysis we kept the 7000 genes with the highest E_i value across samples. Normalization: For most analyses, TPM values in the matrix were normalized according to $= \log 2\left(\frac{\mathrm{TPM}}{10} + 1\right)$. The values were divided by 10 since the actual complexity is assumed to be in the realm of ∼100,000 and not 1 million as implied by the TPM measures. For most analyses the data was centered (each gene was centered across all cells). Centering was done across all samples, or per sample, depending on the analysis.

T Cell Receptor (TCR) Analysis

TCR Sequencing and Clonotype Identification

Bulk TCR beta (*TRBC*) sequencing data was obtained from matched tumor and peripheral blood mononuclear cell (PBMC) samples collected before and after oHSV treatment available at dbGaP under accession number phs003378.v2.p1. These data, generated using the immunoSEQ platform, included metrics of productive rearrangements per ng of input DNA, productive clonality, and template abundance for each sample.

To identify expanded TCR clonotypes, we compared the frequency of each clonotype between pre- and post-treatment samples. Clonotypes were classified as "pre-existing" if detected in both pre- and post-treatment samples, or "emergent" if detected only post-treatment. For pre-existing clonotypes, expansion was quantified as log2 fold change in template abundance per ng of input DNA.

Clonotype selection for Xenium probe design

For spatial tracking, we selected the 15 most expanded pre-existing clonotypes and 10 most abundant emergent clonotypes from each of two patients (P28 and P34) who demonstrated robust T cell responses. Custom Xenium probes were designed targeting the CDR3 regions of selected clonotypes. These probes were engineered with left and right halves spanning the V and J genes respectively, with ligation occurring in the middle of the CDR3 region to ensure high specificity for individual TCRs.

TCR screening against public databases

We screened only expanded clonotypes, defined as either pre-existing clones with log2 fold-change >1 between post- and pre-treatment tumor samples or emergent clones detected only post-treatment with ≥10 templates (per ng DNA). For each clonotype, we extracted TRB V gene, CDR3 amino-acid sequence, and TRB J gene. Gene names were standardized across datasets by removing

allele suffixes (for example *01), normalizing separators, and collapsing leading zeros to canonical forms. We then performed exact matching on V gene + CDR3 + J gene against human TRB records from VDJdb[22] and McPAS-TCR,[23] and against curated HSV-1[24] and HSV-2 TRB[25] datasets. Matches were deduplicated at the level of sample_id + CDR3β + V + J, and summarized as unique hits per database as well as overlaps across databases. Pathogen annotations from the databases were harmonized to common labels (for example EBV, CMV, Influenza A, SARS-CoV-2, DENV) for reporting. Because only TRB sequences were available for this analysis, some true antigen specificities may be unresolved due to unknown paired TCRα chains.

Spatial Analysis Methods

Proximity Analysis

Cell-to-cell distances were calculated using a nearest-neighbor approach. For each cell, the distance to the three closest cells of a specific type was calculated and averaged. Cells were categorized based on their proximity to other cell types, and distance-based differential expression analysis was performed to identify genes and proteins that correlated with spatial location.

For HSV proximity measurements the number of neighbors was set to 20 to identify putative focal HSV detection rather than potential background staining.

Cellular Neighborhood Analysis

Cellular neighborhoods were identified using an approach adapted from Schürch et al.,[46] that considered both cell phenotypes and their spatial relationships. First, a cell-cell interaction network was constructed based on proximity. Then, neighborhoods were defined as regions enriched for specific patterns of cell-cell interactions. This analysis identified distinct cellular neighborhoods, including tumor-dominated, tumor – T cell interface, vasculature-rich, peri-necrotic, and lymphoid aggregate regions.

HSV Detection

Immunohistochemistry of HSV

HSV immunohistochemistry was performed on an FFPE section adjacent to a CODEX section. Anti-herpes simplex virus type 1 (rabbit polyclonal, Agilent, Cat# B0114) was used. The HSV immunohistochemistry slides were scanned at 20X magnification. HSV immunohistochemistry images were spatially registered with CODEX images to analyze the relationship between residual viral protein and immune cell infiltration.

Viral Transcript Detection

HSV transcripts were detected in Xenium data using custom probes targeting key viral genes. Cells were classified as HSV-positive if they contained at least one viral transcript.

QUANTIFICATION AND STATISTICAL ANALYSIS

Paired and unpaired statistical tests were used as appropriate: Wilcoxon signed-rank tests were used for paired comparisons, and Mann-Whitney U tests for unpaired comparisons. For fold change analyses, log2 fold changes were calculated per sample with pseudocount adjustment (1 for cell density or 0.001 for other measures), and fold changes across samples were tested against zero using Wilcoxon signed-rank tests to determine significance of enrichment or depletion. Correlation analyses were performed using Spearman correlation coefficients. Survival analyses utilized Kaplan-Meier methods with log-rank tests. Statistical significance is indicated either by p values in the figures, or denoted as: $^{*}p < 0.05$, $^{**}p < 0.01$, $^{***}p < 0.001$; p values less than 0.05 were considered statistically significant.

ADDITIONAL RESOURCES

CODEX User Manual Rev_C used for CODEX antibody staining and image data acquisition: https://www.akoyabio.com/wp-content/uploads/2021/01/CODEX-User-Manual.pdf

Xenium user guide

https://www.10xgenomics.com/support/in-situ-gene-expression/documentation/steps/assay/xenium-prime-in-situ-gene-expression-with-optional-cell-segmentation-staining-user-guide

Code for CODEX data processing pipeline:
https://github.com/DFCI-CODEX-group/CODEX-custom-pipeline

Code for full analysis of CODEX and Xenium: https://github.com/maximemeylan/GBM_CAN3110

Clinical trial NCT03152318 registration: https://clinicaltrials.gov/study/NCT03152318

CellPress
OPEN ACCESS

Supplemental figures

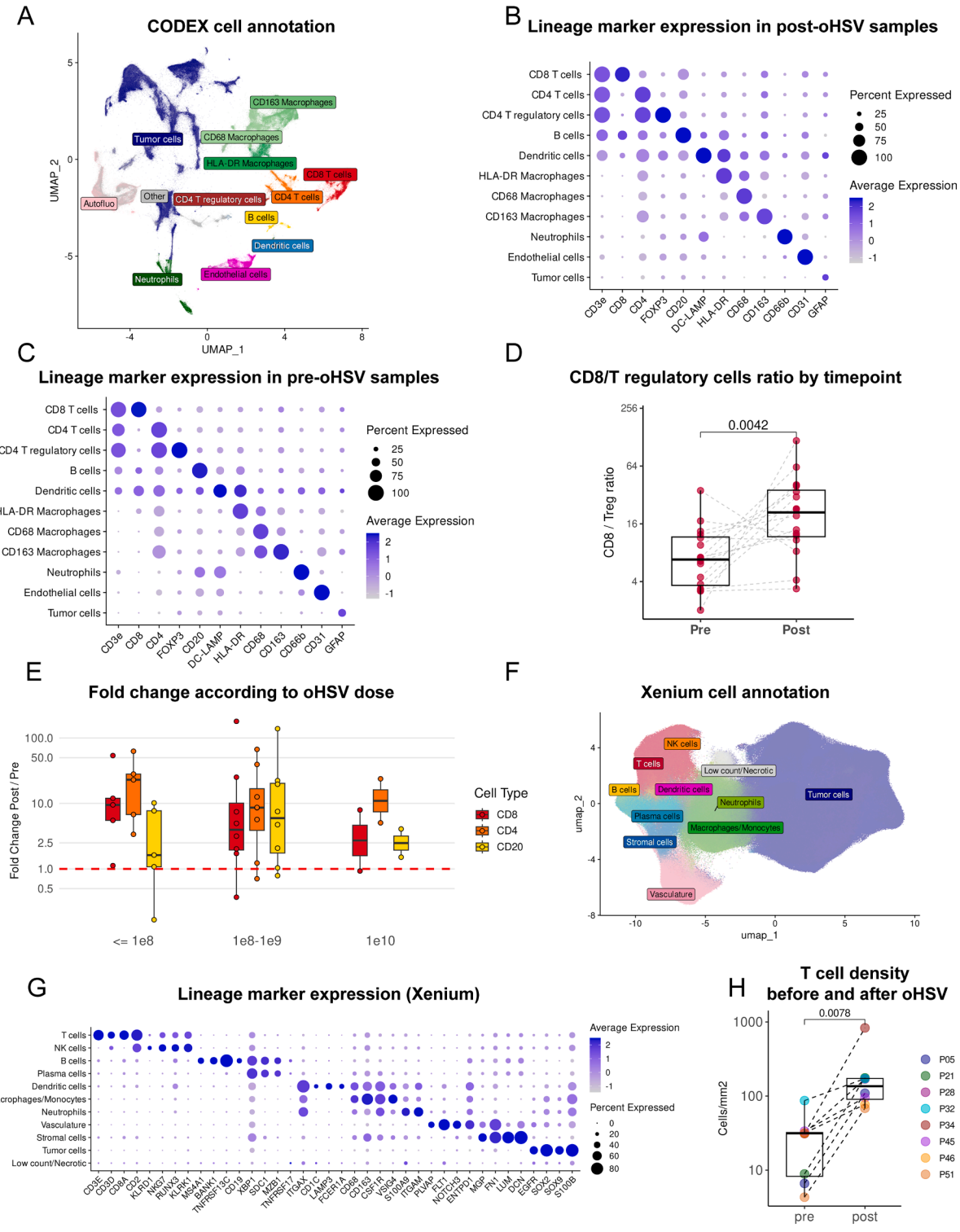

(legend on next page)

Figure S1. CODEX and Xenium annotation and cell-type distribution, related to Figure 1

(A) UMAP of CODEX cell clusters annotated by cell populations.

(B and C) Dot plots of lineage-defining marker expression in CODEX analysis of post-treatment (B) and pre-treatment (C) samples.

(D) Boxplot of CD8 T cell to regulatory T cell ratio by time point. Wilcoxon signed-rank *p* values are shown.

(E) CODEX-based quantification of T cell and B cell densities relative to oHSV dose.

(F) Xenium UMAP showing annotated cell clusters.

(G) Dot plot of lineage-defining marker expression for cell types identified by Xenium spatial transcriptomics.

(H) Boxplot showing T cell enrichment post- versus pre-treatment (Xenium dataset, density per mm^2). Wilcoxon signed-rank *p* values are shown.

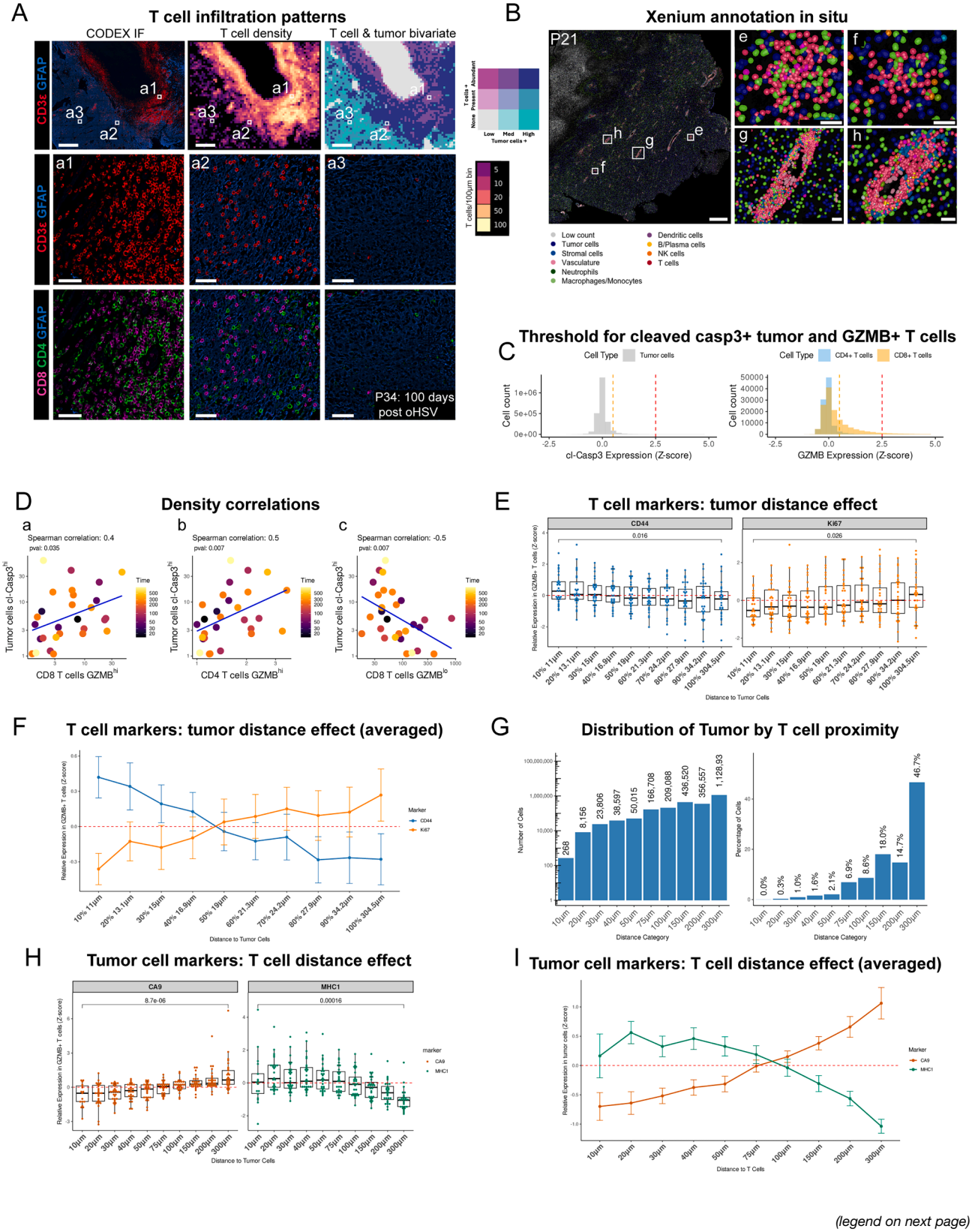

(legend on next page)

Figure S2. GZMB-caspase 3 proximity and spatial gradients, related to Figure 2

(A) CODEX composite figure of resection sample P34 collected at 100 days post oHSV. Three regions are shown: (a1) lymphoid aggregate, (a2) tumor-T cell interface, and (a3) tumor core. The top middle plot shows a heatmap of CD3ε$^+$ T cell density (cells per 100 μm^2 bin). The top right plot shows bivariate maps of T cell versus tumor cell density, highlighting spatially heterogeneous yet deeply infiltrating T cell populations. Scale bars: 1 mm (top row) and 50 μm (regions a1–a3).
(B) Xenium images of tumor P21 resected at day 91 post oHSV illustrating interactions of T cells (red) with tumor cells (blue) in the tumor bed (zooms e and f) and formation of lymphoid aggregates (zooms g and h). Scale bars: 1 mm (left panel) and 50 μm (regions e–h).
(C) Histograms of GZMB and cleaved-caspase 3 detection scores used for thresholding.
(D) Scatterplots illustrating significant associations of densities between GZMB^{hi} CD8 or CD4 T cells with cl-Casp3^{hi} tumor cells. Spearman's r and *p* values are shown.
(E and F) Expression of GZMB, CD44, PD-1, and Ki67 in T cells in distance bins relative to tumor cells. Wilcoxon rank-sum *p* values are shown.
(G) Tumor cell distribution (left, number; right, percentage) across T cell distance bins.
(H and I) MHC-I and CA9 expression in tumor cells relative to distance to T cells. Wilcoxon rank-sum *p* values are shown.

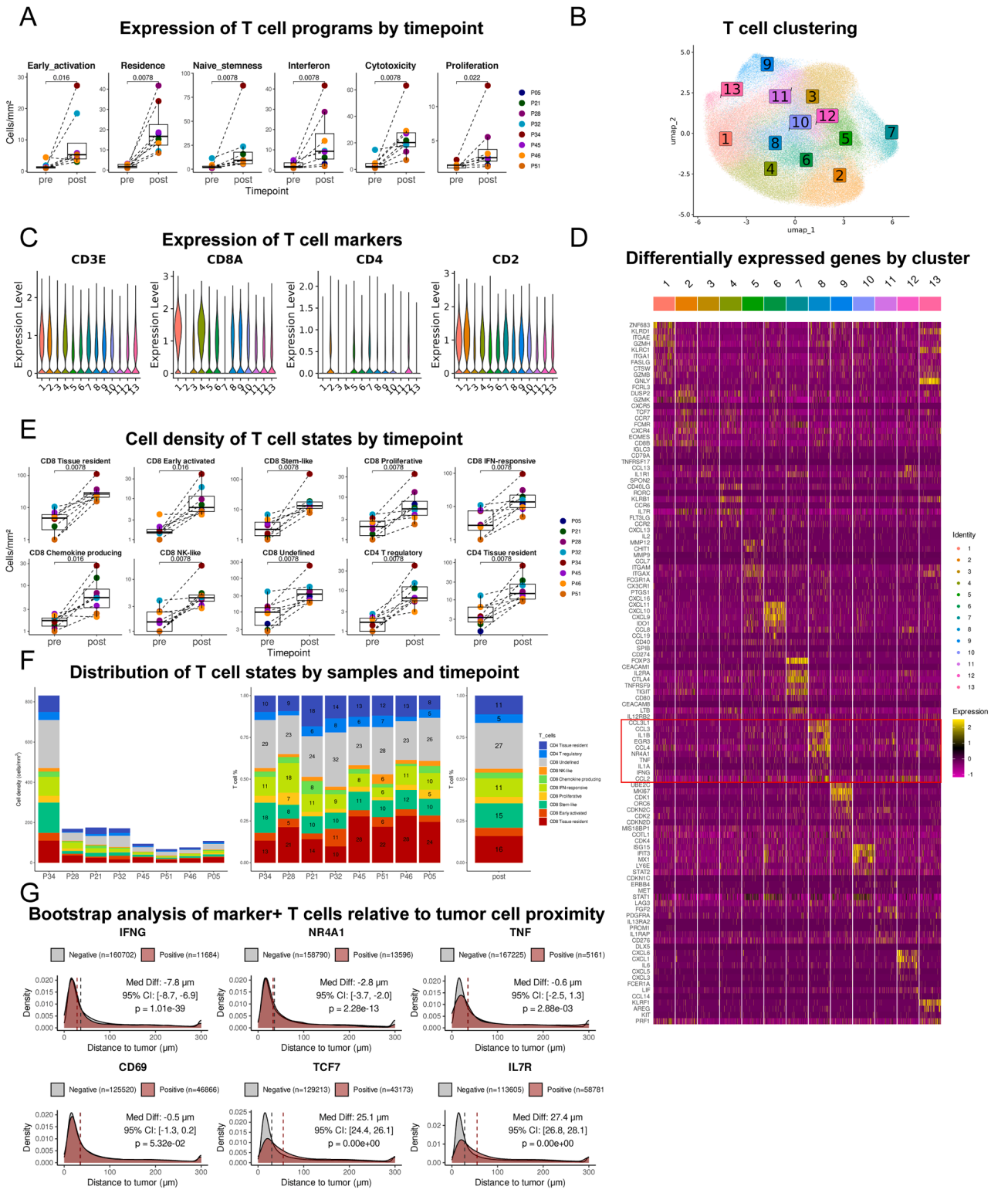

Figure S3. T cell clustering and functional programs, related to Figure 3

(A) Xenium-based enrichment of T cell functional states post-treatment compared with pre-treatment. Wilcoxon signed-rank *p* values are shown.

(B and C) UMAP of T cell clusters and violin plots of marker expression.

(legend continued on next page)

(D) Heatmap showing gene programs across T cell clusters. The red box highlights the cluster of T cells with an early activation program.
(E) Distribution of densities of T cell states in pre- versus post-treatment specimens Wilcoxon signed-rank *p* values are shown.
(F) Representation of T cell state abundance and proportions post-treatment.
(G) Proximity to tumor cells for marker-positive and marker-negative T cells. Median differences with 95% bootstrap confidence interval and Wilcoxon rank-sum adjusted *p* values are shown.

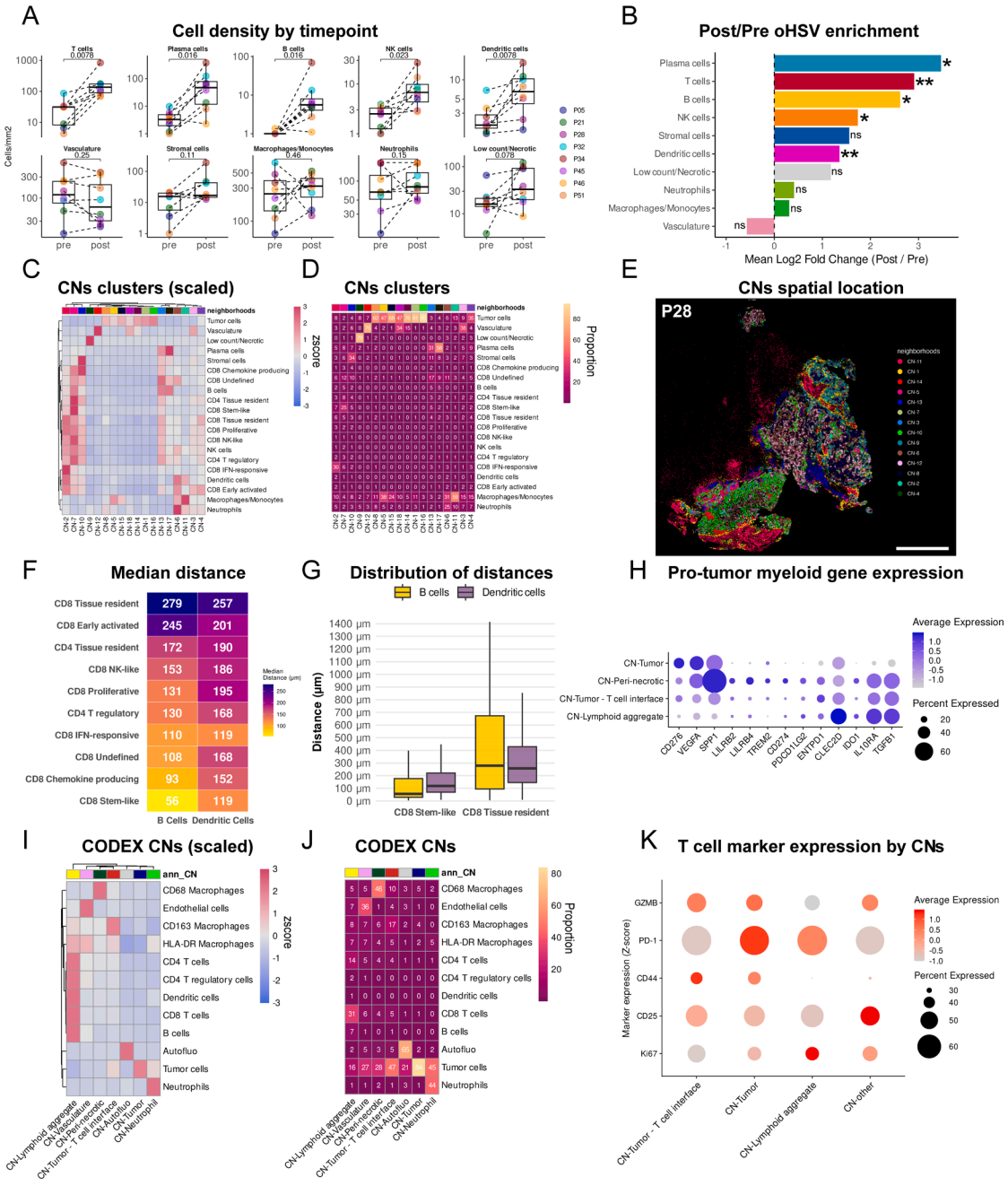

Figure S4. Spatial organization of CNs, related to Figure 4

(A and B) Immune cell-type enrichment in post- versus pre-treatment specimens. Adjusted Wilcoxon rank-sum *p* values shown (A), log2 fold changes tested against zero using Wilcoxon signed-rank tests.

(C and D) Heatmaps representing the 17 initial CNs prior to grouping and annotation (Xenium dataset).

(E) Composition of initial CNs for tumor P28 post oHSV. Scale bar: 2.5 mm.

(F) Median distance of each T cell state to dendritic cells and B cells.

(G) Distribution of distances to dendritic cells and B cells for CD8 stem-like and CD8 tissue-resident T cells.

(H) Expression of genes associated with immunosuppressive functions of macrophages/monocytes according to their spatial location in CNs.

(I and J) Cell composition of CODEX-based CNs analysis as normalized values (I) or proportions (J).

(K) Dot plot of T cell markers in CODEX CNs.

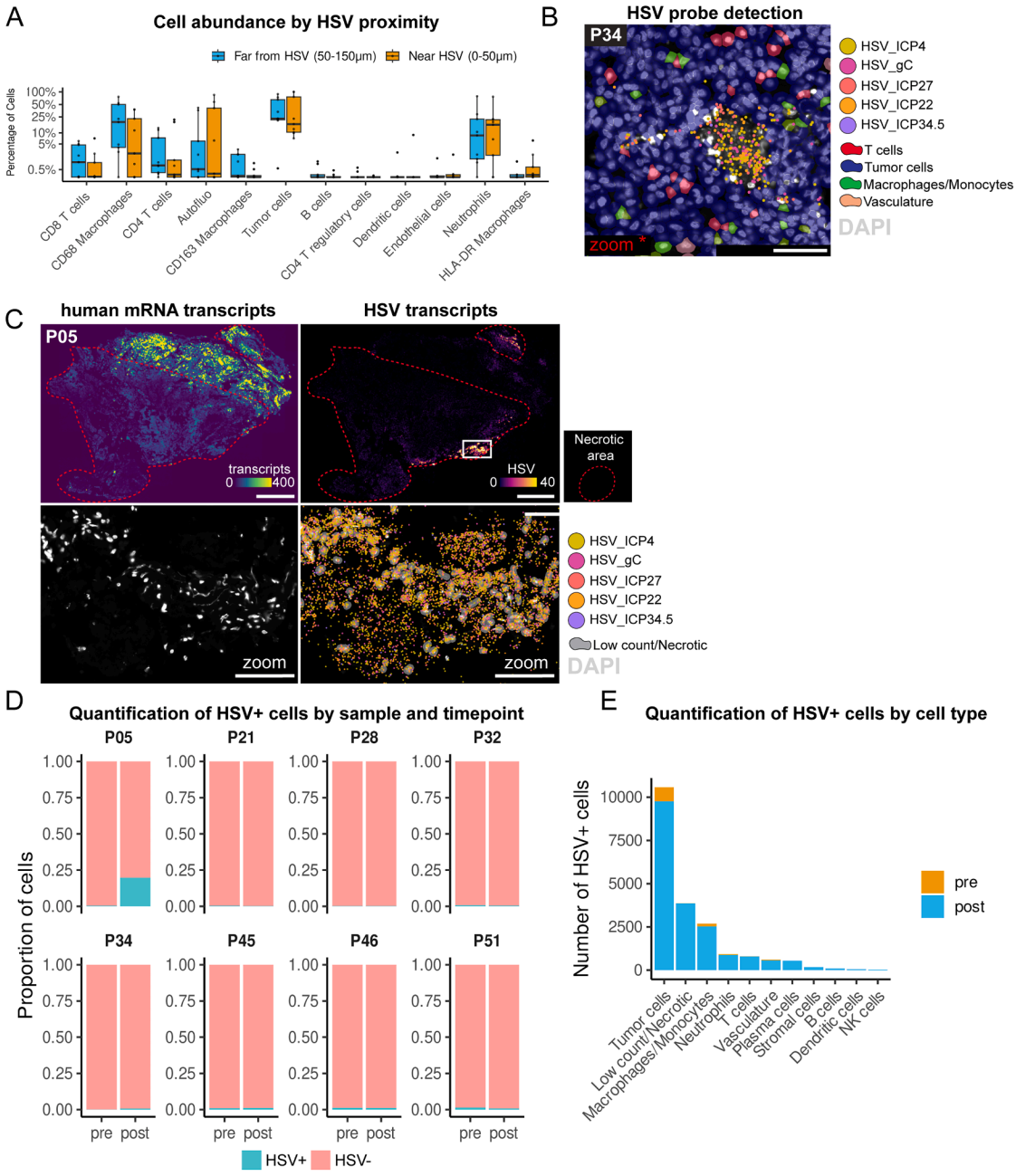

Figure S5. HSV detection and immune cell composition in proximity to residual virus, related to Figure 5

(A) CODEX cell-type distribution based on distance from HSV⁺ areas.

(B) Zoom of a focal HSV⁺ area from Figure 5C, showing individual HSV gene targets in necrotic tumor cells (absence or fragmented DAPI labeling). Scale bar: 50 µm.

(C) Xenium detection of HSV transcripts in necrotic areas characterized by low cellular transcript abundance (red dotted lines) for the P05 post-treatment sample. Scale bars: 1 mm (top row) and 100 µm (bottom row).

(D and E) HSV transcript count distribution by sample, time point (D), and cell type (E).

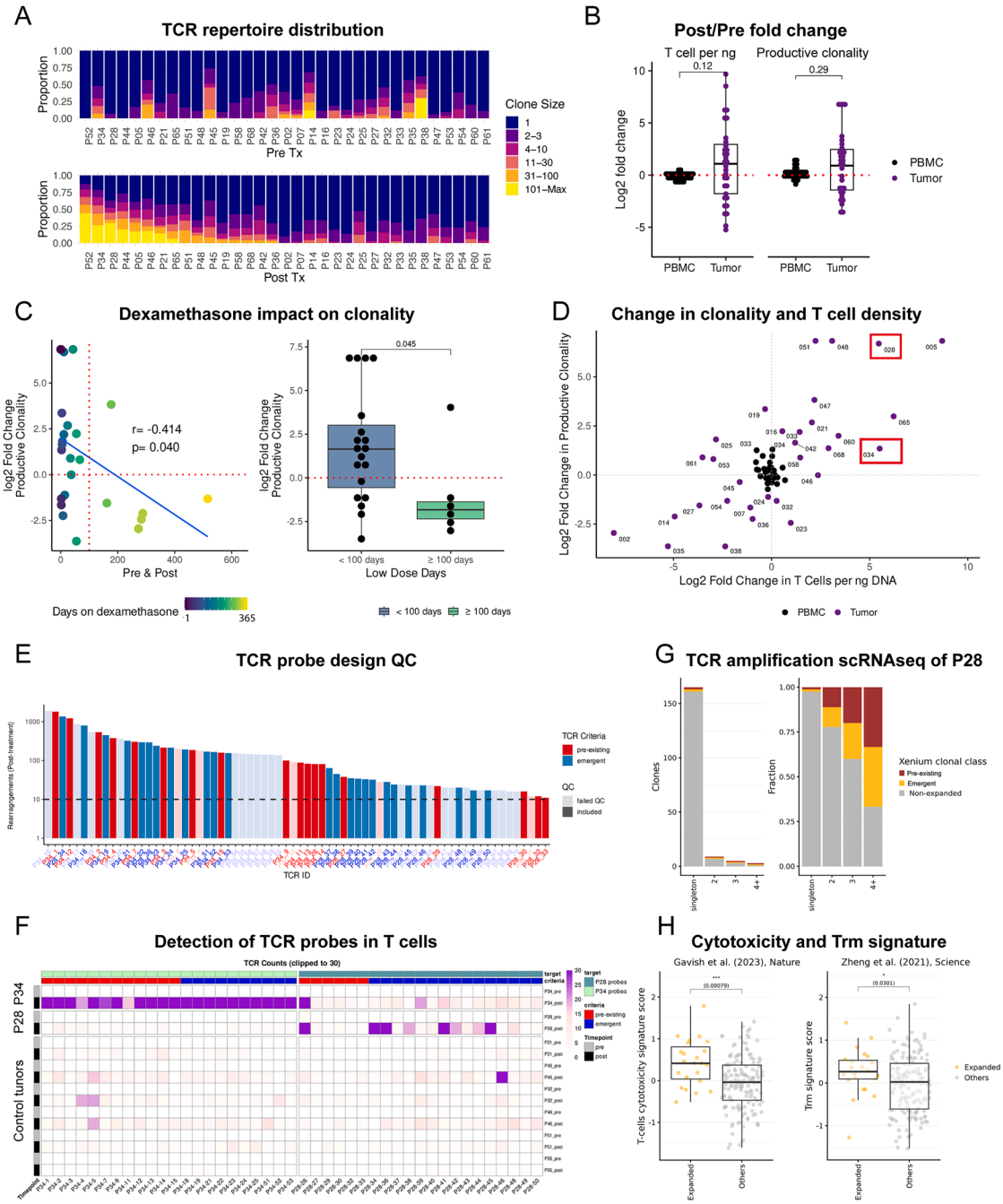

Figure S6. TCR sequencing and Xenium probe validation, related to Figure 6

(A) Bar plots showing the proportion of the T cell repertoire occupied by clonotypes counted multiple times in tumor samples.

(B) Log_2 fold change between post- versus pre-treatment specimens for T cells (per ng of gDNA) and productive clonality for PBMC and tumor samples. Wilcoxon signed-rank *p* values are shown.

(C) Impact of dexamethasone treatment duration on T cell productive clonality. Pearson's r and *p* values (left) and Wilcoxon rank-sum *p* values (right) are shown.

(D) Selection of post-treatment tumor samples P28 and P34 (red boxes) featuring substantial fold change enrichment in clonality and T cell density for spatial mapping by Xenium.

(E) QC and abundance of TCR clonotypes (from bulk TCRβ-seq analysis) included in Xenium panel.

(legend continued on next page)

(F) Quantification of expanded TCR clonotypes detected by Xenium spatial transcriptomics in patients P28 and P34, with control samples (P05, P21, P32, P45, P46, and P51) demonstrating probe specificity and minimal cross-reactivity.
(G) Confirmation of expansion status of selected TCR clonotypes for patient P28 using scRNA-seq-based TCR analysis.
(H) Cytotoxicity and tissue-resident memory gene signature enrichment in expanded versus non-expanded TCR clones for patient P28 (scRNA-seq). Wilcoxon rank-sum *p* values are shown.

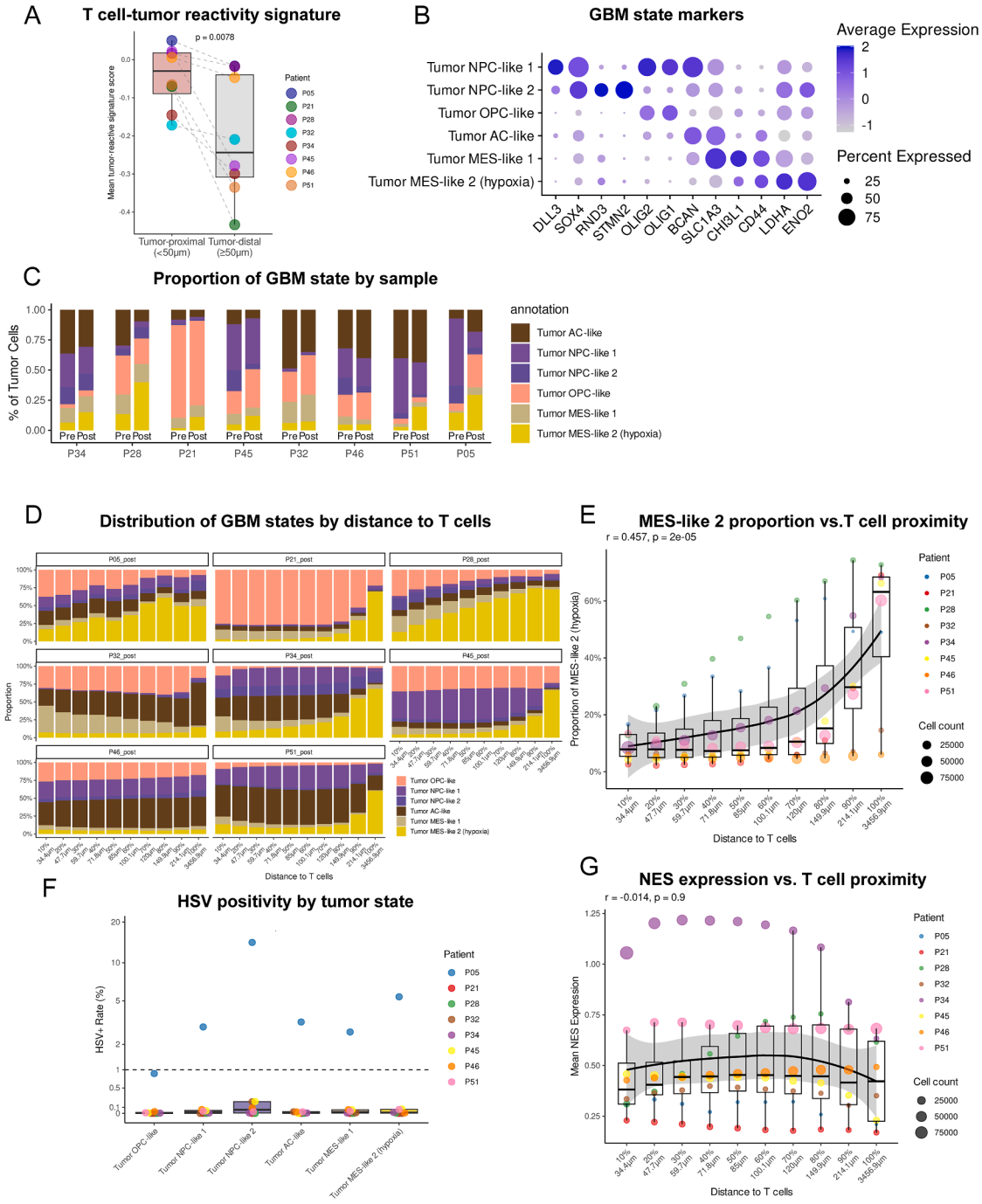

Figure S7. Tumor cell state distribution relative to distance to infiltrating T cells, related to Figure 7

(A) Boxplot showing tumor-reactive signature score in T cells positioned close (<50 μm) or distant from tumor cells (>50 μm) across eight post-treatment Xenium samples. Tumor-reactive signature was based on *CXCL13*^{high}, *ENTPD1*^{high}, *ZNF683*^{high}, *ITGAE*^{high}, *IL7R*^{low}, and *TCF7*^{low}. Wilcoxon signed-rank *p* values are shown.

(B) Dot plot showing marker expression validating tumor cell state classification for the Xenium assay.

(C) Tumor cell state composition across samples at pre- versus post-treatment time points.

(D) Tumor cell state proportions according to proximity to T cells for each post-treatment sample.

(E) Correlation of the proportion of MES-like 2 tumor cells with distance to T cells for each post-treatment sample. Spearman's r and *p* values are shown.

(F) Proportion of HSV-positive tumor cells according to their molecular state.

(G) Correlation of the nestin (*NES*) expression in tumor cells with distance to T cells for each post-treatment sample. Spearman's r and *p* values are shown.